FEM SIMULATIONS OF CONTINUOUS WAVE LASER MACHINING PROCESSES ON A 3-AXIS MILLING MACHINE

by

ALEXANDROS GOSTA

Electrical Engineer

A THESIS

submitted in partial fulfillment of the requirements for the degree

MASTER OF SCIENCE

DEPARTMENT OF ELECTRONIC ENGINEERING

SCHOOL OF ENGINEERING

HELLENIC MEDITERRANEAN UNIVERSITY

2025

Abstract

This study explores the modeling and simulations of laser-metal interactions using a high-power Continuous Wave (CW) fiber laser system. Advanced thermal-structural finite element method (FEM) simulations, which provide detailed analyses of the laser-material interaction process, are employed. Temperature gradients, displacement fields, stress and strain evolution and distributions, are simulated to provide insights into the dynamic material response from low to high (2kW) energy regimes. By simulating both elastoplastic and thermal effects from elastic to ablation regimes, the study identifies critical process thresholds, including the required laser power density and irradiation duration for static and dynamic laser machining applications such as marking, etching, engraving, and cutting. The models follow the experimental setup which integrates a 2 kW TRUMPF CW laser assembled with a 3-axis CNC milling machine through a specialized optical system. The simulation results are compared with CW laser machining experimental results performed in parallel by S. Kamposos whose thesis was performed in collaboration with A. Gosta. The contributions of this work expand the knowledge base for developing predictive modeling techniques in laser manufacturing processes and optimizing their industrial applications.

Table of Contents

Abstract iii
Table of Contents iv
List of Figures v
List of Tables viii
Acknowledgements ix
1. Lasers in machining and manufacturing 1
1.1 Introduction to lasers 1
1.2 FEM modeling of laser machining and manufacturing 2
2. FEM modeling and simulations 4
2.1 Introduction to FEM 4
2.2 FEM simulation software 8
2.2.1 LS DYNA 8
2.2.2 High Performance Computer (HPC) ARIS GRNET 9
2.3 Modeling and simulation 11
2.3.1 Mathematical model 11
2.3.2 Numerical model and simulation parameters 13
2.4 Material selection-material properties of Al 1050 H14 15
3. Diagnostics 20
4. FEM models and simulation results 23
5. Conclusions 43
References 75

List of Figures

Figure 2.1. Mesh geometry of a metal sample modeled using LS-PrePost preprocessor 5
Figure 2.2. CAD Model discretization [14] 6
Figure 2.3. LS-DYNA GUI 9
Figure 2.4. FEM Model with respect to X, Y, Z axis 13
Figure 2.5. Consistent units using LS-DYNA 14
Figure 2.6. Surface Temperature vs Absorptivity of AL 1050 H14 [24] 19
Figure 4.1. The discretized geometry of the model 24
Figure 4.2. Spatial distribution (left) and profile of effective plastic strain from 25
Figure 4.3. Temperature spatial distribution (left) and temperature vs time (right) 25
Figure 4.4. Simulated displacement results (left) compared to white light interferometry results (right) 26
Figure 4.5. Simulated temperature distribution results (left) compared to temperatures measured by the thermal camera (right) 27
Figure 4.6. Simulated temperature distribution results, at a given distance of $\Delta x = 0.7\ mm$ (left), compared to measured temperatures by N-thermocouple (right) 28
Figure 4.8. Representative results of simulation (left) and experiment (right) 30
Figure 4.10. Simulation results of temperature (left), 1 mm from the center of the laser spot, compared to temperature measured by N-thermocouple (right). 31
Figure 4.11. Contour plot of the representative simulation result at t = 200 ms 32
Figure 4.12. Simulated cross-section depth for 250 W (top) and 400 W (bottom) for t=200ms. 33
Figure 4.13. Temperature distribution (left) and simulated temperature vs time graph at a given distance of 1 mm from the irradiation spot 34
Figure 4.14. Simulation result of temperature (left), 1 mm from the center of the laser spot, compared to temperature measured by thermocouple (right) 34
Figure 4.15. Thermal camera measured temperature result (right) compared to corresponding simulation result (left) 35
Figure 4.20. Laser etching and experimental stereoscopic view (left) and FEM temperature distribution 500 ms after the start of laser irradiation (right) 39
Figure 4.21. White light interferometry result retrieved from the experiments [24] 40

Figure 4.22. Measured temperature from the K-type thermocouple versus time (left) and the simulated temperature versus time (right) at a distance 2 mm away from the laser center .. 40
Figure 4.24. a) Image of the cut area from the stereoscope alongside the corresponding FEM simulation result, b) Graph from WLI indicating an approximate cutting width of 300 μm 42
Figure 0.1. Hungarian SZERSZAMGEPIPARI MUVEK Lathe machine 45
Figure 0.2. Lathe machine modified for LAM processes, to hold a collimator (left) vertically to the work area with a DRO (right) to enhance control and precision 46
Figure 0.3. Denford Easimill 3 CNC machine 47
Figure 0.4. Denford's Easimill 3 CNC General Specifications table 48
Figure 0.5. CNC Controller interfaces 49
Figure 0.6. Artsoft's Mach3 interface 50
Figure 0.7. Trumpf's 2000 W High-power CW fiber laser 52
Figure 0.8. Precitec LightCutter 2.0 motorized 3D laser cutting head 53
Figure 0.9. Termotek PU-0600 Chiller 54
Figure 0.10. Trumpf's Fiberview software interface 56
Figure 0.11. Precitec LightCutter 2.0 Motorized 3D laser cutting head, mounted onto a 59
Figure 0.12. Custom-designed bracket using CAD software to vertically mount the Precitec laser cutting head, onto the Denford Easimill 3 CNC machine 60
Figure 0.13. Vertical alignment of the Precitec laser head to the cutting work-bed using a mirror perpendicular to the work-bed to center the reflected beam 61
Figure 0.14. G-Code sample for linear cutting motion movement switching to multiple laser process cycles 63
Figure 0.15. Optris PI-1M thermal camera focused on the irradiated workpiece spot 65
Figure 0.16. Thermocouples mounted on the top surface of the Al workpiece 67
Figure 0.17. Strain gauge construction [22] 68
Figure 0.18. White light interferometry setup [2] 69
Figure 0.19. Leica MZ6 Stereomicroscope 70
Figure 0.20. Laser shots on IR paper were compared to a 250 μm copper sample, ... 71
Figure 0.21. CAD modeled workpiece secured with washer (d=20 mm) and a locking 72
Figure 0.22. The stress applied by the nut on the workpiece caused a displacement of 72
Figure 0.23. Workpiece positioned on top of a metallic grid mesh 73

Figure 0.24. Thermal camera focused at 92 mm distance on a heated needle..... 73
Figure 0.25. Thermal image of a lighter flame showing temperature of 969.9 °C 74

List of Tables

Table 2.1. Material properties of Al 1050 [24] 17
Table 0.1. Mach3 G-code controls used for Laser-CNC operation 63
Table 0.2. Optris PI-1M Technical details 65
Table 0.3. RS PRO Type K & Type N thermocouple specifications 67
Table 0.4. Leica MZ6 stereomicroscope specifications 71

Acknowledgements

I would like to express my sincere gratitude and appreciation to my supervisor Prof. Vasilis Dimitriou for his support and essential guidance during my master thesis, as well for the opportunities he provided me during my studies and for the ones that he continues to provide.

I would also like to thank Asst. Prof. Evaggelos Kaselouris for his continuous support, guidance and insightful feedback throughout the computational studies.

Last but not least, I would like to thank Dr. Ioannis Orfanos, MSc. Eleni Papadaki, Dr. Stelios Petrakis & IPPL scientific staff member MSc. Alexandros Skoulakis for their backend support for providing all the necessary tools and resources in order to successfully complete the necessary master's work. Also, thanks must be given to all researchers and members of IPPL for being very helpful and supportive and of course the Director of IPPL, Prof. M. Tatarakis.

This work was supported by computational time granted from the National Infrastructures for Research and Technology S.A. (GRNET S.A.) in the National HPC facility – ARIS – under project ID pr016025-LaMPIOS_III

1. Lasers in machining and manufacturing

1.1 Introduction to lasers

A laser, or Light Amplification by Stimulated Emission of Radiation, is a device that produces light through optical amplification, based on the principle of stimulated emission of electromagnetic radiation. Unlike other sources of light, lasers generate coherent light, allowing the laser beam to be focused to an extremely sharp point. This property makes lasers exceptionally useful in high-precision applications such as optical communications, laser cutting, and lithography. The high degree of spatial coherence in laser beams enables them to remain strongly collimated over much larger distances, a characteristic crucial for applications ranging from laser pointers to lidar and free-space optical communications.

Apart from spatial coherence, lasers can also exhibit high temporal coherence, enabling them to emit light with a very narrow frequency spectrum. This property is particularly useful when precise wavelength control is required. It also allows for the generation of ultrashort light pulses with broad spectral width but extremely short durations, sometimes as brief as femtoseconds.

Lasers are widely applied across numerous fields and industries. They are critical components in optical disc drives, laser printers, barcode scanners, and DNA sequencing devices. Lasers also play a vital role in fiber-optic and free-space optical communications. In semiconductor chip manufacturing, they are extensively used in processes such as photolithography and etching. In medicine, lasers are employed in surgeries and skin treatments, while in manufacturing, they are indispensable for cutting, welding, and material processing. Military and police applications utilize lasers for tasks such as target tagging, range finding, and speed measurement. In the field of entertainment, laser technology is used to create dynamic lighting and dance shows. In the automotive industry, semiconductor lasers in the blue to near-UV spectrum have begun replacing LEDs in some headlamps due to their higher luminosity and efficiency [1].

Depending on the medium, lasers are divided into following types:

- *Solid-state lasers:* These use a solid crystal or glass as the medium. Examples include ruby lasers and neodymium (Nd) lasers.

• *Gas lasers:* These use a mixture of gases as the medium. Examples include carbon dioxide (CO_2) lasers and helium-neon lasers.

• *Semiconductor lasers:* Commonly known as laser diodes, these are widely used in devices such as CD and DVD players.

• *Dye lasers:* These use organic dyes as the medium, offering the advantage of variable wavelengths.

• *Fiber lasers:* Fabricated from optical fibers doped with rare-earth elements, these are highly valued for applications in telecommunications and high-power operations.

1.2 FEM modeling of laser machining and manufacturing

A laser is a coherent and monochromatic source of electromagnetic radiation that propagates in a straight trajectory with minimal divergence. These characteristics make lasers suitable for a wide range of applications, spanning routine activities and complex scientific investigations. They fulfill both commercial and research purposes and are used in contexts that can be either life-saving or potentially hazardous [2].

High-power lasers, in particular, can produce substantial heat, enabling them to perform various manufacturing and material processing tasks. High-power fiber lasers represent a sophisticated class of solid-state lasers, utilizing rare-earth-doped optical fibers to generate precise and efficient laser beams. These beams are especially suited for applications such as cutting, welding, and other material processing tasks, with significant relevance in the aerospace and automotive industries. The effectiveness of machining with fiber lasers strongly depends on operating conditions, which influence the beam's stability, precision, and repeatability. To achieve optimal cut quality, it is recommended to adjust the focal position to the surface or to a depth that maximizes irradiance, corresponding to the material's thickness. Continuous-wave (CW) fiber lasers enable higher cutting speeds than CO_2 and Nd lasers while maintaining a similar cut quality. The position of the focal point within the material is critical, especially for thicker metals, as a slightly wider kerf is required to achieve high-quality cuts with fiber lasers. [3].

Lasers are now extensively utilized in various industrial fabrication methods, supporting everything from mass production of everyday items to highly specialized operations. Laser processing can be applied to a wide range of materials, including metals (from thin foils to thick

sheets), ceramics, glass, polymers, textiles, leather, paper, and wood. A variety of laser sources and processing techniques are employed to address the unique properties of different materials, such as variations in light absorption, hardness, melting and evaporation temperatures, thermal conductivity, and oxidation sensitivity. Each of these factors is evaluated to achieve the desired processing outcomes. Laser material processing has become a pivotal area of laser application, significantly impacting the economy [4].

The complexity of laser-material interactions necessitates precise control, where computers and simulations play a critical role in managing, correcting, and optimizing laser applications within the manufacturing process. Modeling, optimizing, and controlling laser applications is a challenging task, often addressed using computational approaches such as the Finite Element Method (FEM) [5]. FEM is one of the most popular techniques for solving partial differential equations (PDEs) in domains with irregular geometries. Using FEM, engineers can simulate the physical behavior of materials under laser influence, enabling predictions of outcomes such as temperature distribution, mechanical deformation, and potential defects [6-8]. Manufacturers can optimize laser parameters—such as power, speed, and focus—by combining experimental data with FEM simulations, achieving improved efficiency and reduced material waste. Simulations are vital for critical processes such as cutting [9], welding [10], and additive manufacturing [11]. FEM allows the prediction and avoidance of defects, such as cracks, porosity, and distortions, ensuring higher product quality. Consequently, simulations enable manufacturers to determine optimal laser settings for different materials and applications, eliminating the need for time-consuming and costly trial-and-error testing. This computational approach is thus essential for advancing laser material processing, improving accuracy, efficiency, and cost-effectiveness.

2. FEM modeling and simulations

In this chapter the numerical modeling approach employed to model the thermal and mechanical response of metallic materials is presented. Multidimensional, coupled physical problems with spatiotemporal changes are solved by FEM. Model hypotheses, boundary conditions, and significant material properties are addressed. Outputs from simulation are compared with experimental measurements for verification. The goal is to gain a better insight into process parameters and their influence on material performance.

2.1 Introduction to FEM

FEM is a numerical simulation technique used to model and analyze a wide range of engineering and physics problems, including coupled field and multiphysics scenarios [12]. FEM has broad applications in fields such as mechanics, heat transfer, fluid flow, mass transport, and electromagnetism. By decomposing complex systems into small discrete elements, FEM effectively predicts the behavior of materials or structures under specified physical conditions.

FEM works by solving partial differential equations (PDEs) in two or three dimensions, enabling it to accurately represent complex system behavior. Each element in the model represents a small portion of the overall structure, and together, these elements form a mesh that approximates the behavior of the entire system (Figure 2.1). By incorporating defined loading and boundary conditions, FEM can effectively simulate realistic physical effects and analyze quantities of interest, such as displacements, strains, stresses and temperatures within a material.

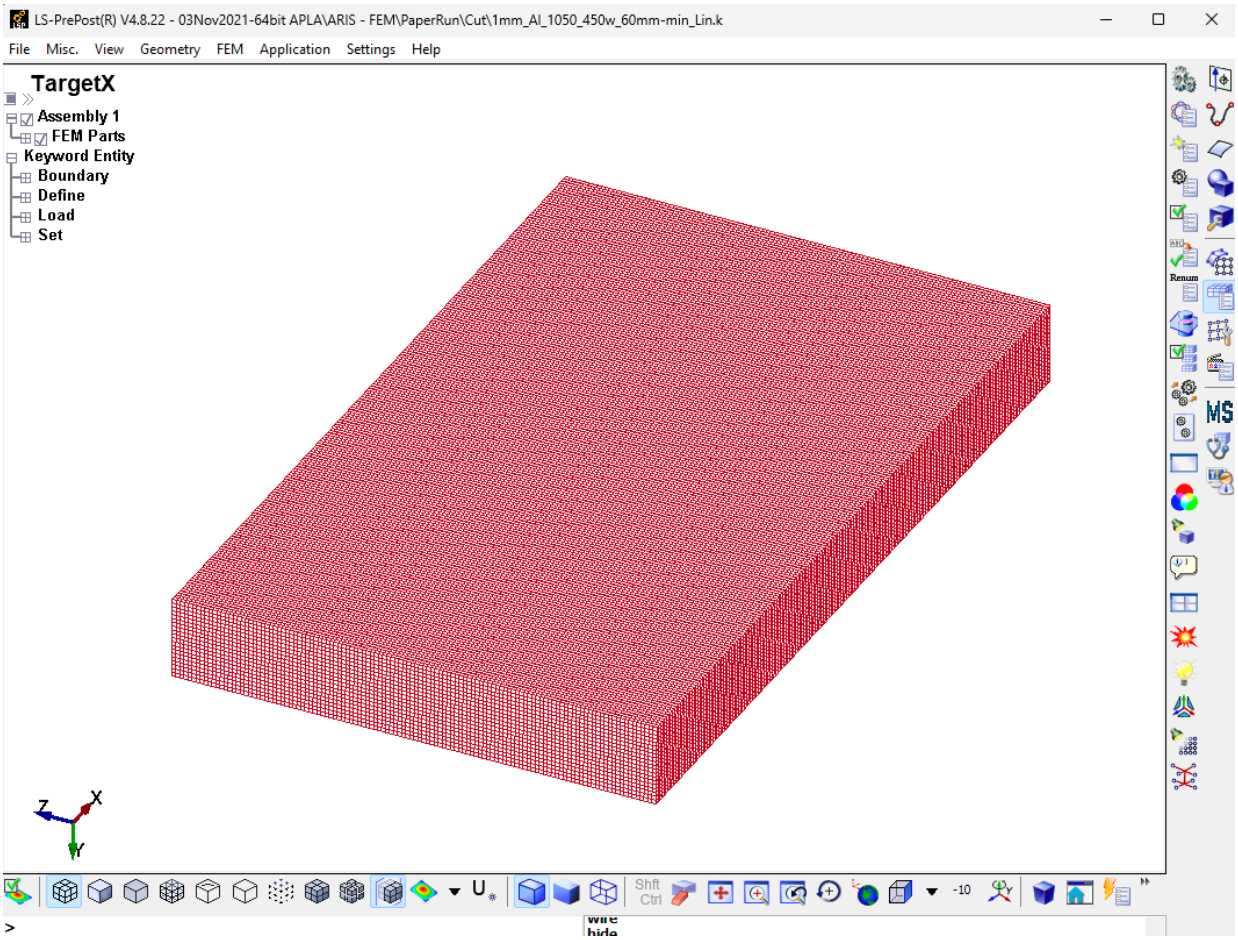


Figure 2.1. Mesh geometry of a metal sample modeled using LS-PrePost preprocessor

Advanced computational power has established FEM as an essential tool for solving complex problems that were previously unsolvable within reasonable timeframes. Today, FEM enables the simulation, optimization, and analysis of systems across diverse applications with unprecedented speed and accuracy. This reduces the reliance on physical prototypes and facilitates easier design improvements. Its ability to handle complex geometries, material properties, and multi-physics interactions has made FEM one of the key technologies in both research and industry.

Fundamentally, FEM works by subdividing a complex physical system into small, simple mesh elements that collectively approximate the behavior of the entire structure (see Figure 2.2). This process converts the complex equations governing material and structural behavior into simpler numerical equations that can be solved computationally. The sequential steps of FEM modeling and simulation are detailed next [13]:

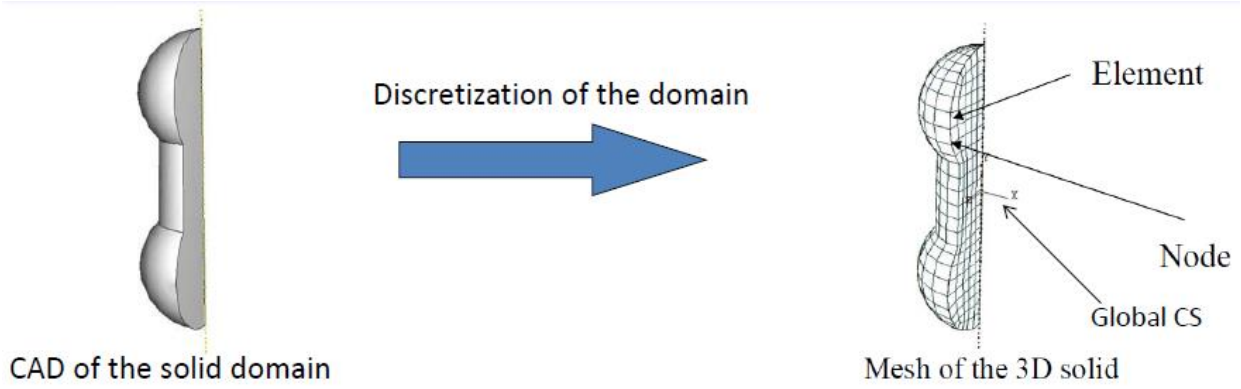


Figure 2.2. CAD Model discretization [14]

- *Discretization of the domain:* This involves subdividing the entire domain, which refers to the material or structure, into a finite number of smaller elements. These elements are typically triangular or quadrilateral in 2D and tetrahedral or hexahedral in 3D. This process creates a mesh of elements that serves as a simplified representation of the real system while retaining sufficient detail to accurately capture its essential behavior.

- *Element Type and Shape Functions Selection:* Each element requires the selection of suitable mathematical functions, known as shape functions, to approximate the behavior of unknown variables such as displacement, temperature, or pressure within the element. These shape functions assume that each variable (e.g., displacement, temperature) follows a predefined variation pattern—typically linear, quadratic, or higher-order polynomial—within the element.

- *Formulation of Governing Equations:* The governing equations are formulated such that each element represents the physical behavior described by PDEs. These equations reflect the underlying physics of the problem, such as elasticity in structural analysis or Fourier's law in heat transfer. By applying shape functions, these PDEs are transformed into algebraic equations, simplifying them into computationally manageable forms.

- *Assembling Global System of Equations:* Once the equations for each individual element have been prepared, they are combined or "assembled" into a global system that represents the entire model. This process ensures connectivity among adjacent elements, allowing the behavior of one element to appropriately influence its neighbors. The outcome is a large matrix that incorporates all interactions and conditions across the elements in the mesh.

- *Boundary/Loading conditions in FEM:* Imposing boundary/loading conditions further constrains the model by applying specific conditions to certain nodes, such as fixed points, applied forces, and temperature constraints, to make the model behave like the real system. These constraints define the limitations on how certain parts of the model can move or respond, aligning the solution with the actual conditions.

- *Solution of the System of Equations:* Once the matrix has been established, the system of equations is solved, typically through matrix inversion or by using iterative numerical methods. Solving these equations provides approximations for the values of the unknown variables at each node.

- *Post-processing and interpretation:* At a later stage, the distribution of quantities such as stresses or temperatures is visualized and interpreted after solving the equations. FEM software typically provides tools to display these results in graphical or contour plot formats, helping understand how the structure behaves under the given conditions.

2.2 FEM simulation software

Today, simulation has become the cornerstone of modern industry, revolutionizing product design, testing, and optimization. Simulations reduce the need for physical prototypes, save time, and free up resources to explore complex scenarios with high precision. FEM simulation has long been applied across various industries, including automotive, aerospace, manufacturing, and energy, to enhance safety, efficiency, and product performance.

LS-DYNA is an advanced FEM software tool designed for nonlinear dynamics, crashworthiness analysis, large-deformation simulations and Multiphysics [15]. This capability enables industries to simulate complex phenomena, such as vehicle collisions, metal forming, and fluid-structure interactions, with high accuracy. Similarly, ANSYS, COMSOL, and Abaqus are popular software packages used for applications ranging from structural and thermal analyses to electromagnetic and multiphysics coupling.

Such simulations rely heavily on high-performance computing (HPC) systems. HPC enables the simulation of large-scale, computationally intensive models by delivering the parallel processing power required to perform billions of simultaneous calculations efficiently. This capability enables industries to simulate complex systems—such as full vehicle crash tests or an aircraft's aerodynamics—on a practical time scale. Advanced simulation software, combined with HPC infrastructure, empowers industries to innovate, optimize designs, and meet safety and performance standards.

2.2.1 LS DYNA

LS-DYNA (Figure 2.3) is a powerful and versatile finite element analysis (FEA) software tool developed to solve complex nonlinear dynamic problems in real-life scenarios, including large deformations and multiphysics interactions. Developed by Livermore Software Technology Corporation, LS-DYNA is widely used in industries such as automotive, aerospace, manufacturing, and civil engineering. It is primarily applied to tasks related to crashworthiness, impact analysis, and thermal and fluid-structure interaction studies.

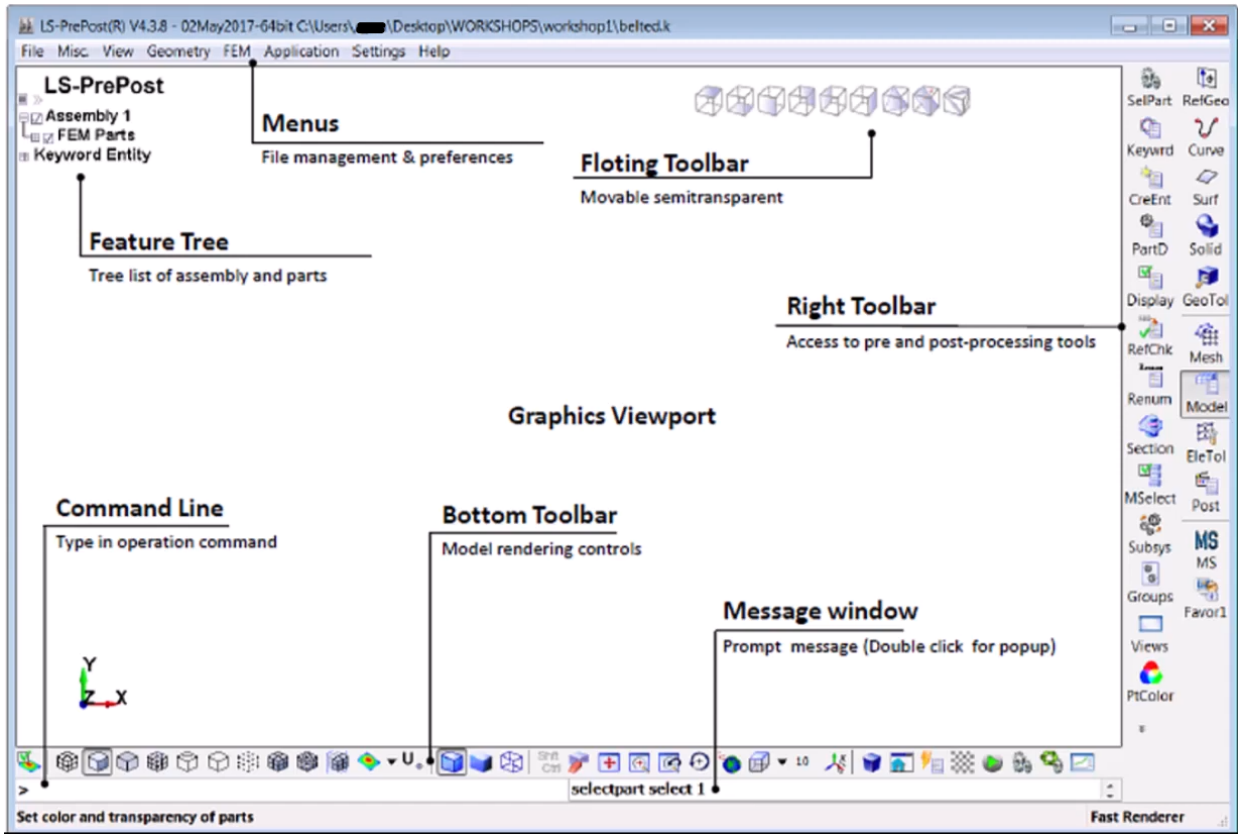


Figure 2.3. LS-DYNA GUI

The power of LS-DYNA lies in its ability to handle nonlinear problems, where material behavior, geometry, or boundary conditions change during a simulation. LS-DYNA offers a wide range of material models and element types, making it suitable for accurately modeling various materials, from metals to polymers, composites, and foams. The software's explicit and implicit solvers allow users to address highly dynamic events, such as crashes or explosions, as well as quasi-static problems like metal forming or structural buckling. LS-DYNA can perform large-scale simulations, including those at very large scales, by taking advantage of powerful parallel computing. Its results are both accurate and computationally efficient [43].

2.2.2 High Performance Computer (HPC) ARIS GRNET

HPC has become a cornerstone for advancing computational research and engineering studies, enabling simulations and analyses of complex systems that would be impossible with conventional computing resources. ARIS (Advanced Research Information System) supercomputer [16] is a cutting-edge HPC infrastructure developed by the Greek Research and

Technology Network (GRNET), meeting today's demanding requirements for state-of-the-art scientific and industrial applications. Powered by advanced multi-core processors, high-speed interconnects, and vast storage capacity, ARIS delivers unparalleled computational performance. It supports highly intensive applications, including climate modeling, bioinformatics, materials science, and engineering simulations.

ARIS utilizes Intel x86 processors and an Infiniband FDR14 interconnect network, ensuring extremely high-speed communication across its computational nodes. The system is organized into five distinct computational islands, each optimized for specific types of workloads and processes:

- *Thin Nodes*: Based on the IBM NeXtScale platform, powered by Intel Xeon E5-2680v2 processors, offering in total, 426 thin nodes which provide 8,520 CPU cores combined for high-performance parallel processing.
- *Fat Nodes*: Optimized for memory-intensive tasks, they run 44 Dell PowerEdge R820 servers. Each of the said servers is powered by 4 Intel Xeon E5-4650v2 processors, each with 512 GB of memory, hence very suitable for applications with high RAM requirements.
- *GPU Accelerator Nodes*: Composed of 44 Dell PowerEdge R730 servers, each equipped with 2 Intel Xeon E5-2660v3 processors, 64GB of memory, and 2 NVIDIA K40 GPUs. They are oriented to the handling of workloads that benefited from GPU acceleration, such as molecular dynamics and deep learning.
- *Xeon Phi Accelerator Nodes*: These consist of 18 Dell PowerEdge R730 servers, each equipped with an Intel Xeon Phi 7120P co-processor, paired with two Intel Xeon E5-2660v3 processors and 64 GB of memory per node. This configuration delivers exceptional performance for highly parallel workloads.
- *Machine Learning Node*: Designed for artificial intelligence and machine learning applications. It provides a single Dell server with 2 Intel Xeon E5-2698v4 processors, 512 GB of memory, and 8 NVIDIA V100 GPUs.

Additionally, the system provides 2 Petabytes (PB) of storage through IBM's General Parallel File System (GPFS). For long-term data storage and archival needs, the infrastructure is complemented by an IBM TS3500 tape library, which offers a maximum storage capacity of 6 PB.

Utilizing ARIS, scientists and engineers can achieve unprecedented levels of accuracy and efficiency in solving problems that demand significant computational power.

2.3 Modeling and simulation

To investigate laser-aluminum material interactions, FEM modeling and simulations were performed. The heating of an Al 1050 workpiece was analyzed during irradiation by a CW fiber laser. Three-dimensional transient coupled thermal-structural numerical simulations were conducted using LS-DYNA software.

2.3.1 Mathematical model

The workpiece is defined as a deformable body. The laser beam is modeled as a Gaussian moving heat source, and for the dynamic elastoplastic behavior of the workpiece, the Johnson-Cook constitutive strength material model was used. The Al workpiece is heated by a Gaussian heat source and is described by the heat conduction equation (1), which also accounts for heat transfer.

$$\rho c \left(\frac{\partial T}{\partial t} + V_x \frac{\partial T}{\partial x}\right) = \frac{\partial}{\partial i}\left(\kappa(T)\frac{\partial T}{\partial i}\right) + \dot{Q} - a_T T_0 (3\lambda + 2\mu)\dot{\varepsilon}_{ii} \quad (1)$$

Where:

i=x,y,z coordinates, t time

ρ the density, c the specific heat, V_x the laser scanning speed along the x-direction

k thermal conductivity and the power generation per unit volume

T temperature, T_0 ambient temperature, α_T thermal expansion coefficient,

λ, μ lame coefficients, strain rate

Intense heating causes rapid thermal expansions, generating a stress field and ultrasonic waves that propagate through the material [17]. This wave propagation is described by the 3D transient mechanical equation (2), which incorporates strain (3) and stress (4) tensors to represent the mechanical behavior of the solid target.

$$\rho \frac{\partial^2 U_i}{\partial^2 t} = \mu \frac{\partial^2 U_i}{\partial^2 k} + (\lambda + \mu) \frac{\partial}{\partial i}\left(\frac{\partial U_k}{\partial k}\right) - (3\lambda + 2\mu)\alpha_T \frac{\partial T}{\partial i} \quad (2)$$

Where:

U the displacement, ρ the density, λ *and* μ lame coefficients, α_T thermal expansion coefficient.

The strain tensor:

$$\boldsymbol{\varepsilon_{ij}} = \frac{\mathbf{1}}{\mathbf{2}}\left(\frac{\partial U_i}{\partial U_j} + \frac{\partial U_j}{\partial U_i}\right) \quad (3)$$

The stress tensor:

$$\boldsymbol{\sigma_{ij}} = \mathbf{2}\boldsymbol{\mu}\boldsymbol{\varepsilon_{ij}} + \boldsymbol{\lambda}\boldsymbol{\varepsilon_{kk}}\boldsymbol{\delta_{ij}} - (\mathbf{3}\boldsymbol{\lambda} + \mathbf{2}\boldsymbol{\mu})\boldsymbol{\alpha_T}(\boldsymbol{T} - \boldsymbol{T_0})\boldsymbol{\delta_{ij}} \quad (4)$$

Finally, the volumetric laser heat source is represented as a Gaussian distribution of the absorbed laser heat flux or laser power intensity, as described by:

$$Q(\boldsymbol{x},\boldsymbol{y},\boldsymbol{z}) = \frac{\boldsymbol{P_{tot}}}{\boldsymbol{\pi r_b^2 H}} * \left(\mathbf{1} - \frac{\boldsymbol{y}}{\boldsymbol{H}}\right) * \boldsymbol{e}^{-\left(\frac{(z-z_0)^2+(x-x_0)^2}{r_b^2}\right)} \quad (5)$$

where P_{tot} is the total absorbed power and r_b is the laser beam radius and H is the thickness of the workpiece. It holds that:

$$P_{tot} = \eta P_{inc} \quad (6)$$

where P_{inc} is the incident laser power, and η is the average absorptivity of the Al workpiece.

The motion of the laser beam is along the X-axis (see Figure 2.4). The focused CW laser beam diameter is 250 μm with laser power ranging from 0.2 to 1 kW.

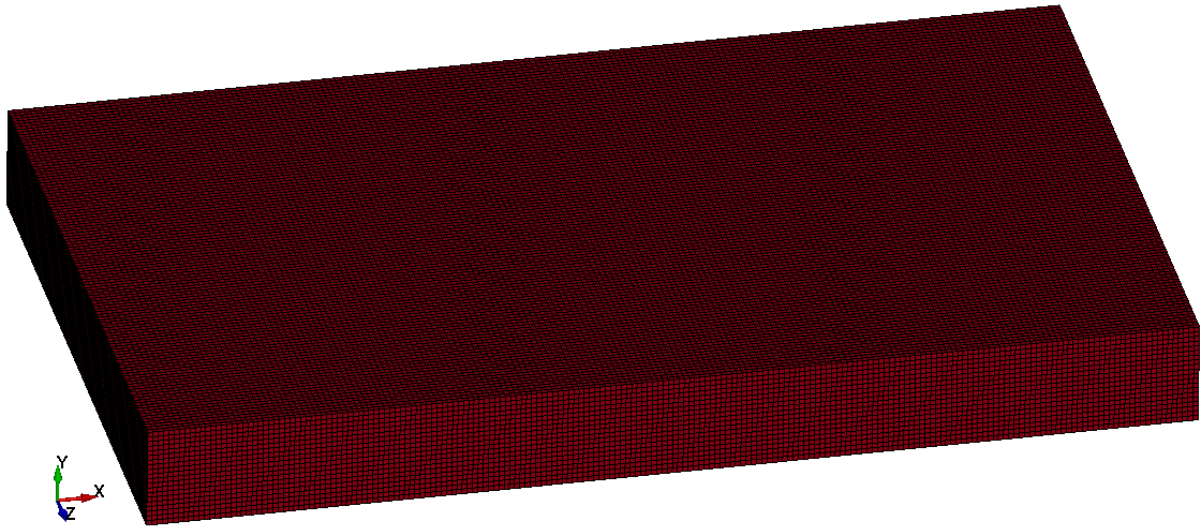


Figure 2.4. FEM Model with respect to X, Y, Z axis

2.3.2 Numerical model and simulation parameters

The consistent units used for the simulations are described in Figure 2.5. A rectangular Al solid with dimensions of 10 mm × 6 mm and a thickness of 1 mm is modeled using 480,000 solid finite elements (Figure 2.4). Non-reflecting outflow boundary conditions are applied to the outer areas of the workpiece, except the upper one where the thermal source is applied, and the ambient temperature is set to 20 °C. The bottom XZ plane was fully constrained. The 3D transient coupled thermal-structural FEM simulation runs at the GRNET HPC, ARIS. A typical run uses 1 core and 20 nodes and needs approximately 5 hrs to be completed for a 500 ms simulation time.

MASS	LENGTH	TIME	FORCE	STRESS	ENERGY	DENSITY	YOUNG's	35MPH 56.33KMPH	GRAVITY
kg	m	s	N	Pa	J	7.83e+03	2.07e+11	15.65	9.806
kg	cm	s	1.0e-02 N			7.83e-03	2.07e+09	1.56e+03	9.806e+02
kg	cm	ms	1.0e+04 N			7.83e-03	2.07e+03	1.56	9.806e-04
kg	cm	us	1.0e+10 N			7.83e-03	2.07e-03	1.56e-03	9.806e-10
kg	mm	ms	KN	GPa	KN-mm	7.83e-06	2.07e+02	15.65	9.806e-03
g	cm	s	dyne	dy/cm²	erg	7.83e+00	2.07e+12	1.56e+03	9.806e+02
g	cm	us	1.0e+07 N	Mbar	1.0e+07 Ncm	7.83e+00	2.07e+00	1.56e-03	9.806e-10
g	mm	s	1.0e-06 N	Pa		7.83e-03	2.07e+11	1.56e+04	9.806e+03
g	mm	ms	N	MPa	N-mm	7.83e-03	2.07e+05	15.65	9.806e-03
tonne	mm	s	N	MPa	N-mm	7.83e-09	2.07e+05	1.56e+04	9.806e+03
lbf-s²/in	in	s	lbf	psi	lbf-in	7.33e-04	3.00e+07	6.16e+02	386
slug	ft	s	lbf	psf	lbf-ft	1.52e+01	4.32e+09	51.33	32.17
kgf-s²/mm	mm	s	kgf	kgf/mm²	kgf-mm	7.98e-10	2.11e+04	1.56e+04	9.806e+03
kg	mm	s	mN	1.0e+03 Pa		7.83e-06	2.07e+08		9.806e+03
g	cm	ms		1.0e+05 Pa		7.83e+00	2.07e+06		9.806e-04

Figure 2.5. Consistent units using LS-DYNA

The main keywords used in LS-DYNA to structure this simulation are here described:

- CONTROL_ENERGY: Used to specify the controls for energy dissipation options
- CONTROL_SOLUTION: Used to define solution control (thermal, structural, both) and output parameters
- CONTROL_TERMINATION: Used to specify the problem termination time, time between timesteps & number of timesteps
- CONTROL_THERMAL_NONLINEAR: Used to specify thermal nonlinear control parameters
- CONTROL_THERMAL_SOLVER: Used to specify thermal analysis solver type as well as the thermal analysis type
- CONTROL_THERMAL_TIMESTEP: Used to specify thermal time interval used to update the temperature distribution in the model as heat is generated, conducted and convected during the transient thermal analysis simulation
- CONTROL_TIMESTEP: Refers to the timestep, a fundamental parameter that determines the size of each time increment in the simulation

- DEFINE_CURVE: Used to define material curves or loading curves for various types of analysis to describe the behavior of materials, boundary conditions, and other physical parameters that change over time or with respect to specific variables
- DEFINE_FUNCTION: Used to define user-defined functions that can be used to specify time-dependent or state-dependent behaviors in the simulation
- EOS_LINEAR_POLYNOMIAL: Defines the material behavior for solids undergoing large deformations, such as in impact or explosion simulations. Represents the relationship between the pressure (P) and the specific volume (V) of the material
- LOAD_HEAT_GENERATION_SET_SOLID: Used to specify a heat generation rate for a solid element. It is used to simulate the heat generated by friction, plastic deformation and other sources
- MAT_ADD_EROSION: Used to simulate the removal of material due to erosion
- MAT_ADD_ THERMAL_EXPANSION: Used to simulate the expansion of materials due to temperature changes
- MAT_JOHNSON_COOK: Used to simulate the behavior of materials under high strain rates and high temperatures and the deformation and failure of materials under these conditions
- MAT_THERMAL_ISOTROPIC_PHASE_CHANGE: Used to simulate the thermal behavior of materials undergoing phase change, to simulate the melting and solidification of materials

2.4 Material selection-material properties of Al 1050 H14

For the material selection, commercially recognized materials with a uniform distribution of properties across their surface were prioritized. This approach increases the likelihood of obtaining consistent experimental data and measurements, thereby enhancing the validation of simulation-experiment results.

Aluminum alloy Al 1050 H14 was selected for this study due to its status as a commercially pure aluminum alloy, widely known for its excellent corrosion resistance, high thermal conductivity, superior electrical conductivity, and good formability. The "H14" designation

indicates that the alloy is strain-hardened to achieve medium strength without requiring additional heat treatment. Furthermore, it retains aluminum's inherent advantages, such as ductility, ease of machining, and improved mechanical properties. These characteristics make Al 1050 H14 particularly well-suited for applications requiring lightweight materials, especially in industries such as electrical, chemical, and architectural sectors, where corrosion resistance is also critical. A comprehensive understanding of the mechanical, thermal, and other key properties of Al 1050 H14 is essential for its integration into simulations utilizing FEM. This knowledge is expected to facilitate accurate simulations and optimization in a range of manufacturing processes involving Al.

The dynamic elastoplastic behavior of the workpiece is described by the Johnson-Cook constitutive strength material model, which accounts for the effects of plastic strain, strain rate, and temperature. The flow stress is expressed as:

$$\boldsymbol{\sigma = (A + B\dot{\varepsilon}^{n})(1 + Cln\frac{\dot{\varepsilon}}{\dot{\varepsilon}_0})(1 - \frac{T-T_r}{T_m-T_r})^{m}} \quad (7)$$

where $\dot{\varepsilon}$ is the equivalent plastic strain, is the dimensionless plastic strain rate, $=1s^{-1}$ is a reference strain rate used to normalize the strain rate, T_m is the melting temperature of the workpiece and T_r the room temperature. The material constants A, B, C, n, m given in Table 2.1 are determined from literature experimental results.

The coupling between thermal and mechanical effects is crucial. The thermal field (temperature distribution) influences the mechanical behavior by affecting the material's yield strength, while mechanical deformation can alter thermal conductivity and heat dissipation in localized regions due to changes in density or microstructure. This coupled thermo-mechanical analysis provides insights into the material's response, such as the extent of the heat-affected zone (HAZ), the onset of plastic deformation or fracture, and potential material failure under extreme conditions, which is described by the Johnson-Cook fracture model

$$\boldsymbol{\varepsilon_f = (D_1 + D_2 e^{D_3\frac{p}{\sigma_{VM}}})(1 + D_4 ln\frac{\dot{\varepsilon}}{\dot{\varepsilon}_0})(1 + D_5\frac{T-T_r}{T_m-T_r})} \quad (8)$$

$$\boldsymbol{D = \Sigma\frac{\Delta\varepsilon}{\varepsilon_f}} \quad (9)$$

where p is the pressure, D1, D2, D3, D4, and D5 are the failure parameters of the material, specifically, D_1 the initial failure strain, D_2 the exponential, D_3 the triaxility, D_4 the strain rate, D_5 the temperature factors, and σ_{VM} is the Von Mises stress. When the failure parameter D becomes 1, the material fractures. T_m is the melting point, and $\dot{\boldsymbol{\varepsilon}}$ and $\dot{\boldsymbol{\varepsilon}}_0$ are the plastic strain rate and reference strain rate, respectively. The material model includes the fracture model in case of high strain rates, and it is defined by the previous equations.

Key properties of Al 1050 H14 (Table 2.1) include:

- Density: Approximately 2.71 g/cm³, making it lightweight and ideal for weight-sensitive applications.
- Thermal Conductivity: High thermal conductivity (~229 W/mK) ensures efficient heat dissipation, which is particularly beneficial for heat exchanger and electrical applications.
- Electrical Conductivity: Excellent electrical conductivity (~59% IACS) makes it a preferred material for components used in electrical and power distribution systems.
- Corrosion Resistance: Exceptional resistance to corrosion in diverse environments, including atmospheric exposure and certain chemical conditions, owing to the high purity of the aluminum.

Table 2.1. Material properties of Al 1050 [26-41]

Property	Value	Property	Value
Tensile strength:	100 [MPa]	n (strain hardening exponent):	0.42
Yield strength:	75 [MPa]	m (thermal softening exponent):	1.34
Elongation:	~10%	Specific heat:	898.7 [J/kg*kelvin]
Density:	2.71 [kg/m^3]	Melting point:	650 [°C]
Young modulus:	68 [GPa]	Thermal conductivity (20 °C):	222 [W/mK]

Bulk modulus:	75 [GPa]	Latent heat:	400 [Joule/gr]
Shear modulus:	26 [GPa]	D1 (fracture parameter):	-0.77
Poisson ratio:	0.33	D2 (fracture parameter):	1.45
λ (1st Lame coefficient):	25.46 [Pa]	D3 (fracture parameter):	-0.47
μ (2nd Lame coefficient):	26.10 [Pa]	D4 (fracture parameter):	0.0
A (initial yield of the material):	324 [MPa]	D5 (fracture parameter):	1.6
B (strain hardening coefficient):	114 [MPa]	Liquidus temperature:	657 [°C]
C (strain rate sensitivity):	0.002	Solidus temperature:	646 [°C]

In terms of mechanical properties, Al 1050 H14 exhibits moderate tensile strength, typically in the range of 100–120 MPa, with an elongation at break of approximately 10–15%. This allows for significant forming without the risk of fracture. While its hardness is lower compared to higher-strength aluminum alloys, this characteristic facilitates easier machining and bending without cracking, making it suitable for applications requiring complex shapes or intricate components. Moreover, temperature dependent properties for thermal conductivity and specific heat were considered [18], as well as the coefficient of thermal expansion for Al 1050 H14 is considered, approximately $24 \times 10^{-6}\ \mathrm{K}^{-1}$, which is relatively high and should be accounted for in applications involving temperature fluctuations.

The uniform properties of Al 1050 H14 across its surface are primarily attributed to its high purity and minimal alloying elements. This results in consistent mechanical and physical characteristics throughout the material, ensuring reliability for applications demanding homogeneity, such as thin foils, reflective surfaces, and cladding. The absence of significant alloying elements also minimizes variability in hardness and density, ensuring that surface treatments, coatings, or finishes adhere evenly.

Due to its excellent formability and uniform properties, Al 1050 H14 is widely used in applications involving bending, rolling, or other forming processes, such as sheet metal work, automotive trim, heat exchangers, and chemical storage [42]. In simulations using FEM, the alloy's uniform and predictable properties enable accurate modeling. This is particularly advantageous

when simulating thermal responses or deformation under stress, where consistent material behavior across the surface is critical.

The most significant aspect in these simulations was the absorptivity coefficient, since the ambient atmospheric conditions (surface roughness, finger stains, debris) can make the Al surface absorptivity to vary. Based on [24] the experimental measurements denote an absorptivity value of ~30%, as shown in Figure 2.6. The absorptivity coefficient similarly to other metals, like AA 1100, also changes along with the surface temperature due to laser radiation [19].

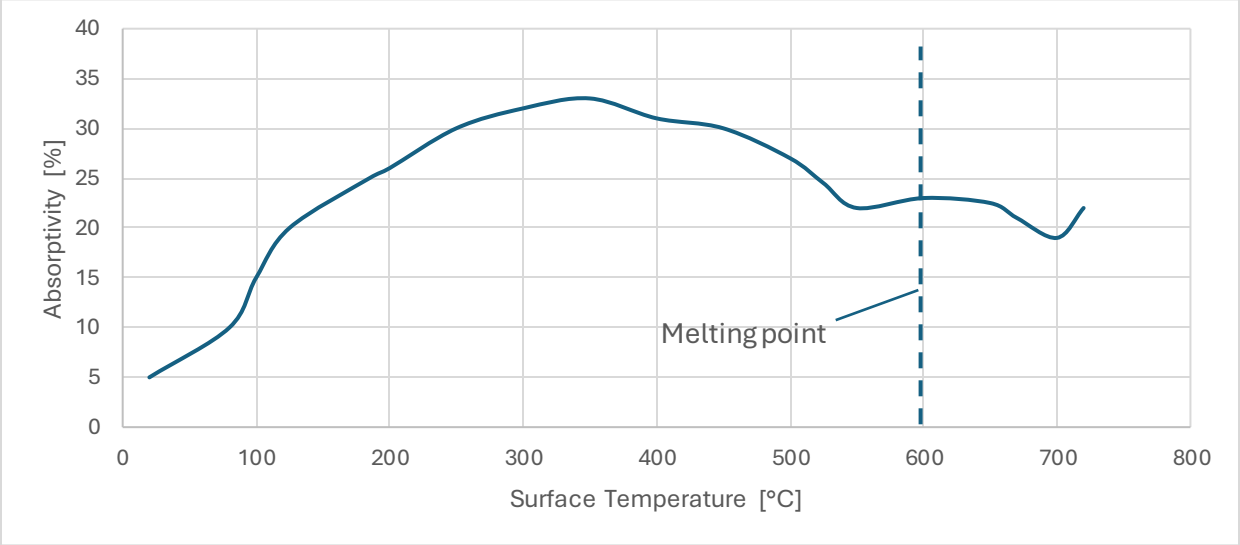


Figure 2.6. Surface Temperature vs Absorptivity of AL 1050 H14 [24]

3. Diagnostics

Diagnostic methods form the core of experimental research and industrial application to enable precise evaluation, monitoring, processing and material properties optimization. Within manufacturing and engineering applications, they ensure quality, performance, and reliability by detecting defects, checking thermal and mechanical performance, and verifying computer modeling. This chapter summarizes all the diagnostic tools used here, describing their operation principles, technical characteristics, and specific roles within the experimental setup. The tools used are thermal imaging systems, thermocouples, strain gauges, white light interferometry, and stereomicroscopy—each component of an integrated diagnostic tool that enables process understanding and material characterization (see Appendix G).

3.1 Thermal camera diagnostics

Infrared thermography is a real-time, non-contact method for temperature distribution measurement on the surface in high-temperature processes. In this study, an Optris PI1M thermal camera (f = 75 mm) is utilized, which is mounted on a CNC machine and targeted the Al 1050 workpiece at a distance of 310 mm. Equipped with notch and long-pass filters to minimize reflections from laser beams, the camera recorded thermal data at the high frame rate of 80 Hz, with adequate spatial and temporal resolution for fine-scale thermal profiling (Appendix G, Figure 5.15).

Calibration is done with material emissivity set to 0.05, and an iris diaphragm was used to further attenuate unwanted reflections. The system provided stable data in a temperature range of 525-1800 °C, depending on the frame rate mode with thermal sensitivity (NETD) of <2 K below 900 °C (Appendix G, Table 5.2). These capabilities enabled accurate investigation of heat distribution and validation of simulation outputs, which are critical in thermal behavior of laser-irradiated materials.

3.2 Thermocouples

To augment the thermal imaging and acquire high-resolution local temperature measurements in the vicinity, K-type and N-type thermocouples are utilized. Positioned 0.5–2 mm from the irradiation spot of the laser, the thermocouples recorded dynamic temperature fluctuations at specific locations (Appendix G, Figure 5.2). This provided a comprehensive temperature profile, particularly near the interaction zone, which is critical for analyzing thermal gradients and their effects on material properties [44].

The thermocouple probes were 0.3 mm in diameter with excellent thermal resistance—up to 600 °C for K-type and 1200 °C for N-type (Appendix G, Table 5.2). The 0.7-second response time of the probes made them particularly suitable for tracking transient thermal phenomena under fast-changing process conditions.

3.3 Strain gauges

Strain gauges are also used in the test setup to track the mechanical response of the material under thermal and mechanical loading. They are based on the measurement of small changes in electrical resistance that are proportional to material deformation. The gauges are bonded directly onto the specimen surface and provided accurate measurements of stress and strain distribution. This measurement is required to understand material behavior at operating loads, to validate stress predictions from simulation, and to optimize process parameters (Appendix G, Figure 5.17) [45].

3.4 White light interferometry

White Light Interferometry (WLI) is a non-contact, high-resolution technique for measuring surface geometry to nanometer accuracy. It functions by splitting a beam of white light such that the interference pattern between the sample and a reference mirror can be used in reconstructing surface geometry. The process is used to measure surface roughness, dimensional variation, and flatness of laser-machined aluminum specimens (Appendix G, Figure 5.18) [46].

WLI's non-destructive nature and spatial precision made it ideal for examining laser-induced surface modifications. Moreover, it contributed to simulation validation by supplying accurate surface data and revealing material response to thermal and mechanical inputs. Its utility in laser processing applications further underscores its importance in both qualitative and quantitative surface analysis.

3.5 Stereomicroscopy

For qualitative analysis, a Leica MZ6 stereomicroscope is employed to visually inspect laser-processed surfaces. Normal optical microscopes observe in two dimensions with one optical path, whereas stereomicroscopes observe in three dimensions with two optical paths, giving improved depth perception. This allowed surface irregularities, microcracks, and other structural defects that could not otherwise be detected with solely quantitative analysis (Appendix G, Figure 5.19). The Leica MZ6 magnification range is 0.63x to 4.0x, with field diameters up to 104.2 mm and working distances up to 297 mm (Appendix G, Table 5.4). These dimensions qualified it for examining laser-processed Al surfaces, as well as interferometric data and facilitating detailed defect analysis [47].

3.6 Diagnostics summary

In combination with several diagnostic tools—thermal cameras, thermocouples, strain gauges, WLI systems, and stereomicroscopes—the experimental process monitoring and material analysis became solidly based. All the tools contributed to the validation of the simulation models and to an overall understanding of thermomechanical responses in laser-material interactions. With the capability to collect thermal, mechanical, and surface data, the combined system delivered a comprehensive, multi-physics characterization of material response for research and industrial process optimization needs. Complete specifications and instrumentation configuration data are provided in Appendix G for reference.

4. FEM models and simulation results

Based on the mentioned CW laser capabilities and the material properties of the Al selection, detailed in chapter 2 and in [24], representative FEM models are developed to simulate the experimental laser machining processes performed and studied in [24]. The thermal and mechanical responses during laser irradiation are herein studied and analyzed. The simulation parameters follow the characteristics and parameters of the laboratory equipment and diagnostics used in the experiments conducted in [24].

4.1 Laser induced plastic deformation forming

This case study analyzes surface plastic deformation induced by a static laser pulse with precisely controlled temporal parameters. The aim is to predict and control the deformation characteristics precisely. The simulation offers insights into optimizing laser parameters to controllably shape the material within its plastic deformation regime.

FEM simulations are performed to model the laser-material interaction under irradiation of a 200 W laser power for 200 ms on a $10 \times 6 \times 1$ mm modeled metal workpiece, discretized using approximately 480,000 solid elements (Figure 4.1). Simulations are performed on HPC-ARIS for an approximate time of 5 hours, utilizing ambient air (no gas assist) at 20 °C. The material properties are defined in Chapter 2 and a mean absorptivity of 32% is used. The simulated results are compared in parallel with the experimental results of [24].

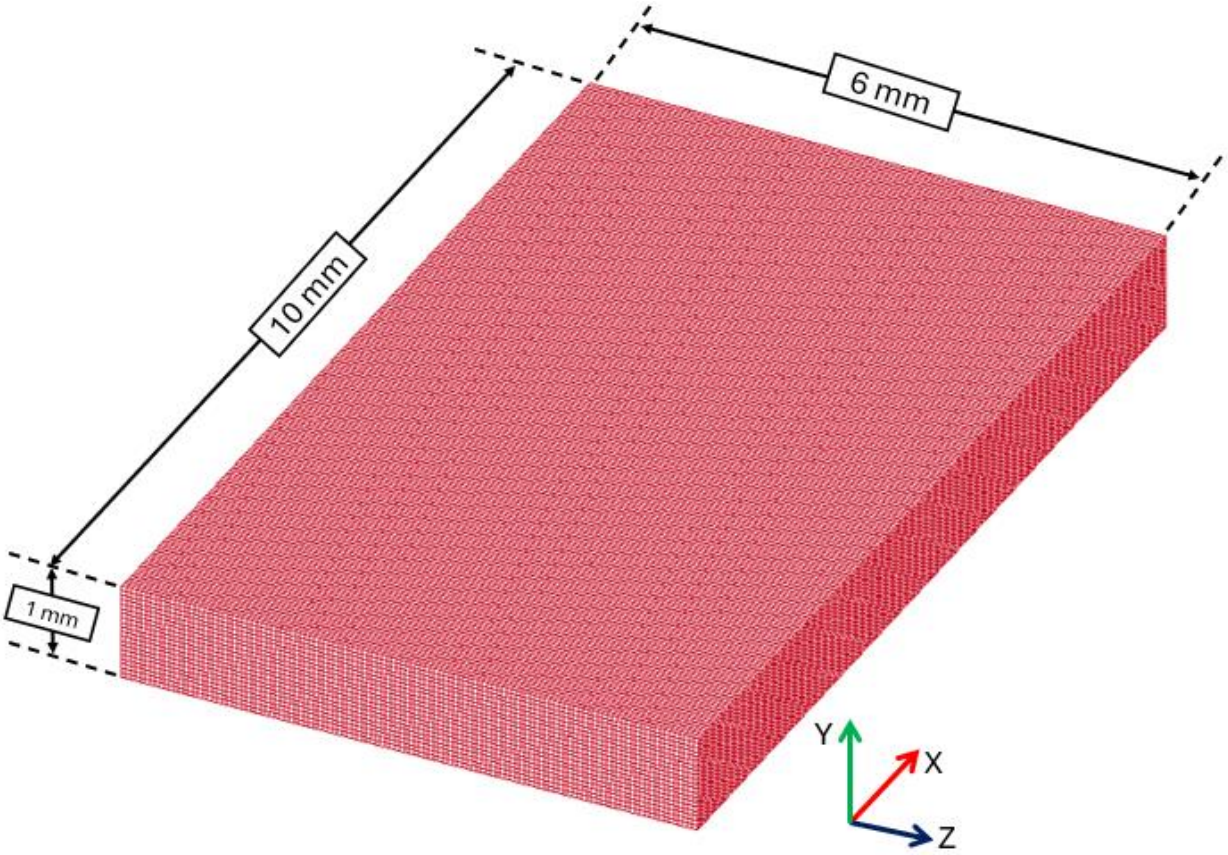


Figure 4.1. The discretized geometry of the model

Representative results are next presented. Figure 4.2 (left) presents a 2D contour plot of the effective plastic strain distribution in space. The deformation pattern is radially symmetric with concentric contours centered. The deformed plastic zone has a diameter of approximately 605 μm. Figure 4.2 (right) is a lineout profile of effective plastic strain vs. distance along the X-axis (mm). The curve shows a double-peaked ("W"-shaped) strain distribution with an amplitude of 4 μm. The profile demonstrates non-uniform plastic deformation, caused by thermal gradients and stress concentration zones.

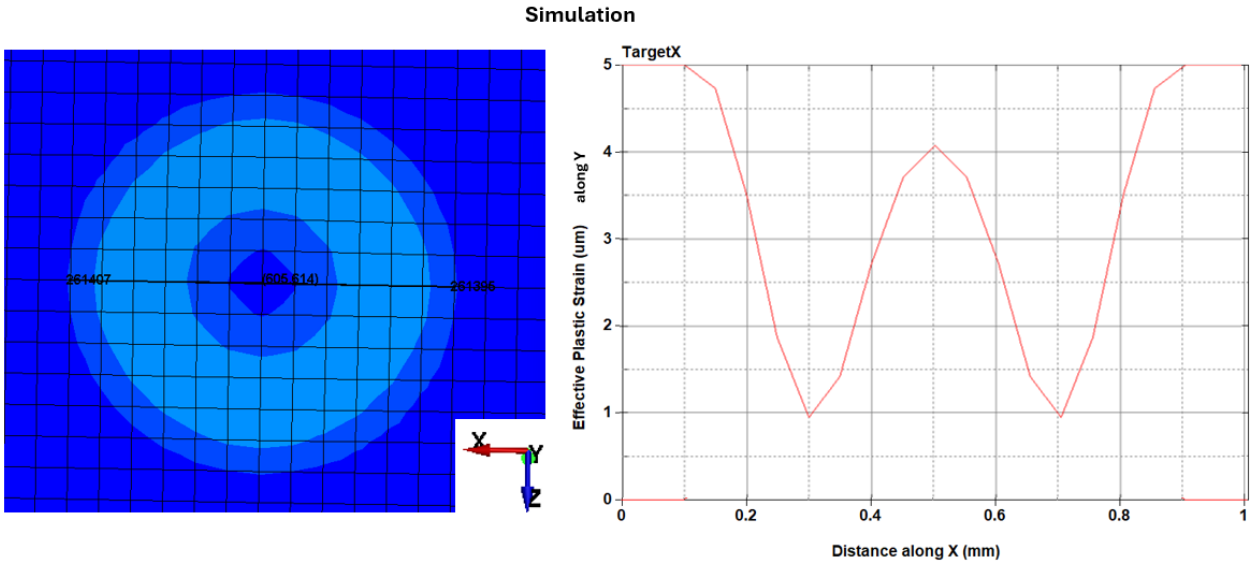


Figure 4.2. Spatial distribution (left) and profile of effective plastic strain from Simulation (right)

The maximum temperature is computed to be approximately 565 °C at the center of the irradiated zone, decreasing gradually to the periphery as low as approximately 54 °C. This temperature gradient is characteristic of a localized energy source and is shown for time = 200 ms. Figure 4.3 (right) illustrates a temperature vs. time plot at a selected node near the irradiation center. Temperature rises very rapidly in the initial stage to nearly 500 °C in the first 50 ms, and subsequently remains with small fluctuations in the range 500–550 °C. This trend reflects transient heating, with the laser-irradiated zone reaching a quasi-steady thermal state.

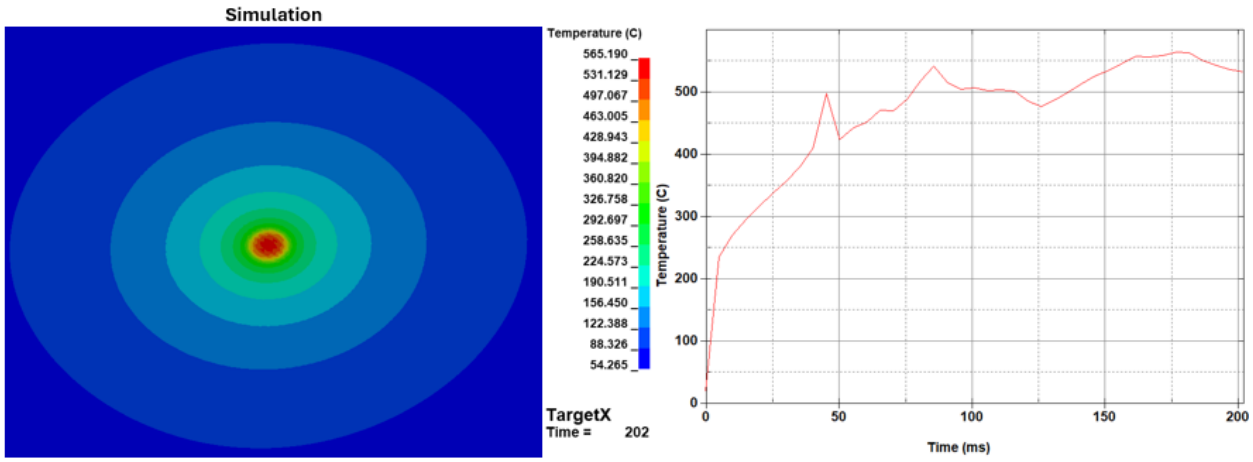


Figure 4.3. Temperature spatial distribution (left) and temperature vs time (right)

Observing the deformed spot from the experimental results [24], no physical deformation appeared through a naked human eye. However, the diameter experimentally measured by white light interferometry, showed good agreement with the simulated results. The experimentally measured permanent deformed spot was ~500 μm in diameter. The computed Y-displacement, showing how much the material expanded upwards, was $\Delta y = 4\ \mu m$. A white light interferometry technique computed the same value of displacement, for a repetition of the same experiment.

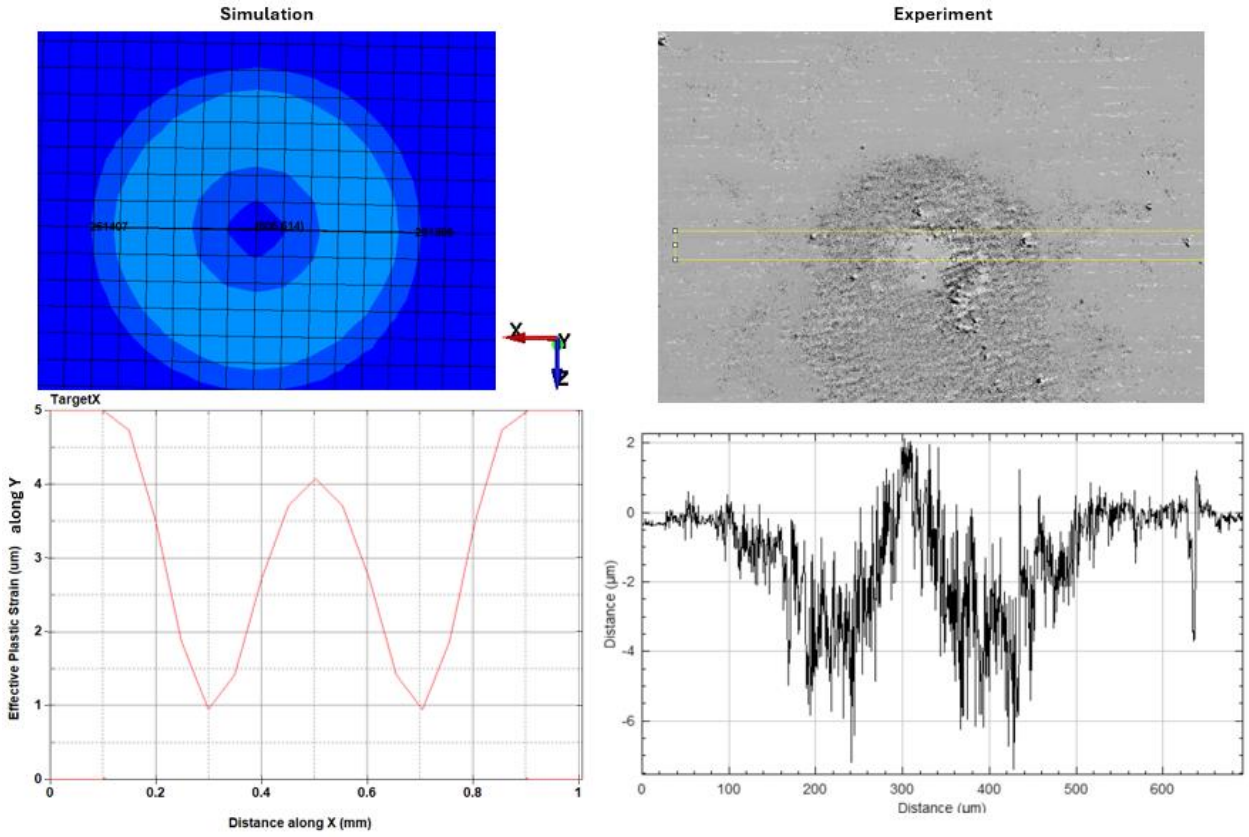


Figure 4.4. Simulated displacement results (left) compared to white light interferometry results (right)

A good agreement is observed, between the simulated thermal distribution results and the experimental results [24]. Not only was the maximum temperature almost the same for both simulation and experiment, but the thermal response also showed great consistency between simulations and experiments. The maximum temperature reached T = 565 °C, for t = 200 ms (Figure 4.5). Additionally, at a distance of 0.7 mm from the center of the irradiated spot, the

simulation predicted a temperature of T = 205 °C (Figure 4.6), while for the same distance the thermocouple measured T = 215 °C, resulting in a percentage difference of 4.6%.

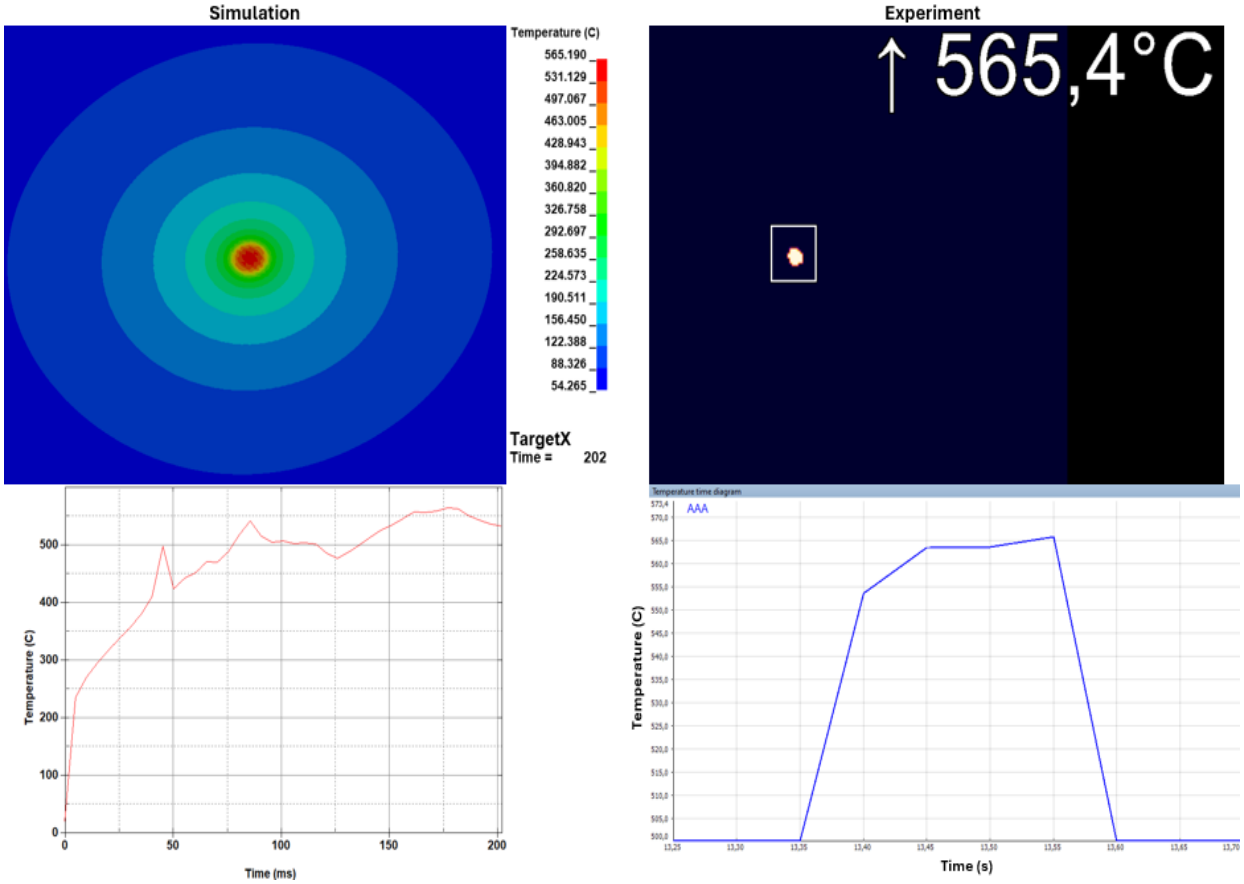


Figure 4.5. Simulated temperature distribution results (left) compared to temperatures measured by the thermal camera (right)

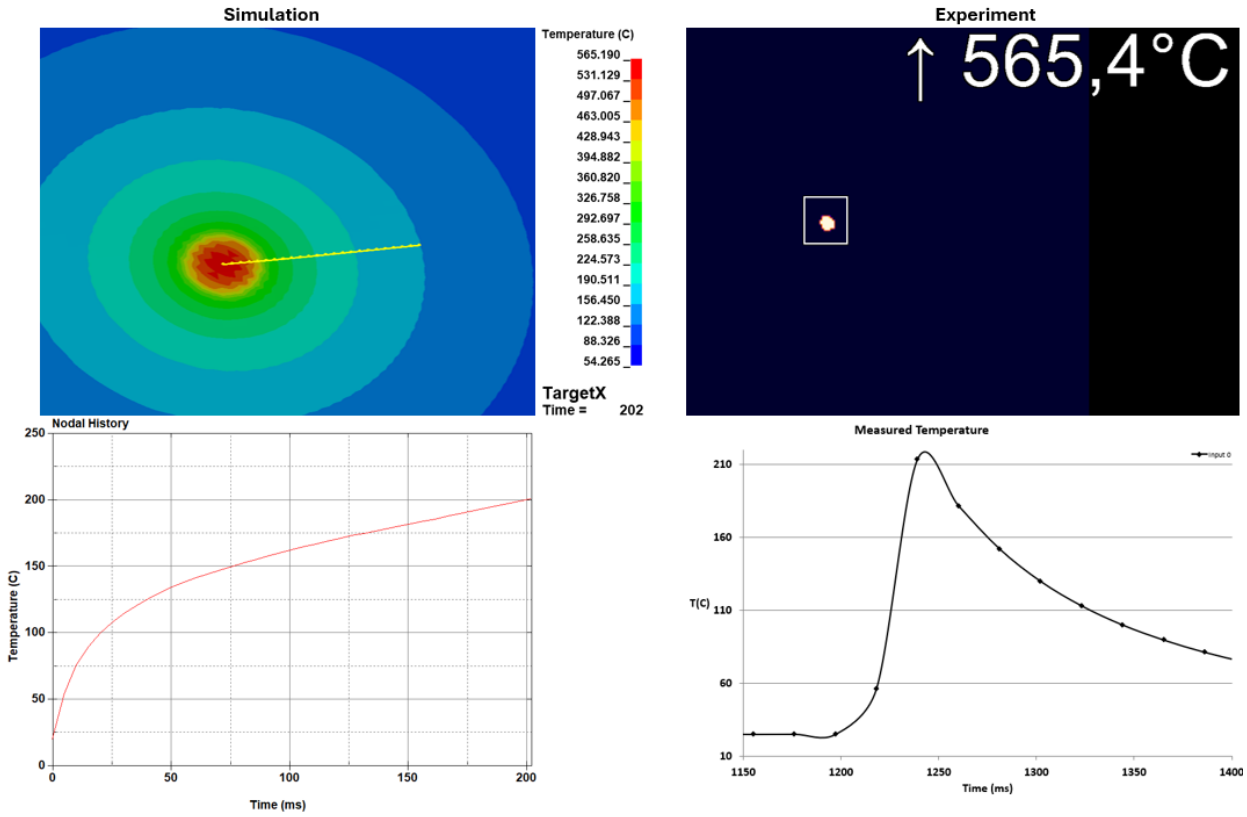


Figure 4.6. Simulated temperature distribution results, at a given distance of $\Delta x = 0.7\ mm$ (left), compared to measured temperatures by N-thermocouple (right)

A common experimental setup is used to further investigate the effects of linear laser movement, in case studies 4.4-4.6, and similarly a thermal camera and thermocouples are used to validate the simulated results [24].

4.2 Laser marking and engraving

This case study investigates the controlled surface marking and engraving by a single pulse, aiming to highlight the relation of material properties and laser parameters while interacting and to demonstrate the capabilities for controllable laser engraving.

FEM simulations are performed to model the laser-material interaction under irradiation of a 250 W laser power for 200 ms on a $10 \times 6 \times 1$ mm metal modeled workpiece, discretized using approximately 480,000 solid elements (**Σφάλμα! Το αρχείο προέλευσης της αναφοράς δεν βρέθηκε.**). The simulation was performed on HPC-ARIS for an approximate time of 5 hours, utilizing ambient air (no gas assist) at 20 °C. The material properties are defined in Chapter 2 and

a mean absorptivity of 37% is used, based on empirical calculation in [24]. The simulated results are compared in parallel with the experimental results of [24]. The boundary conditions and the mesh geometry of modeled metallic sample is the same (depicted in Figure 4.1).

The simulations computed a maximum temperature of 659 °C at 125 ms, which is higher than the previously mentioned case (see section 4.1) of laser induced plastic deformations, exhibiting a faster thermal response.

Figure 4.7 shows representative simulated thermal distribution results at 125 ms from laser irradiation. The inset provides a magnified view of the simulated material failure, revealing a feature measuring 113 µm in width and 250 µm in depth. The right graph is a temperature vs. distance plot. Simulation results indicate a temperature of 659 °C at. Material failure is initiated at 125 ms, while the temperature is calculated to be 240 °C at a radial distance of 1 mm from the center of the irradiated spot.

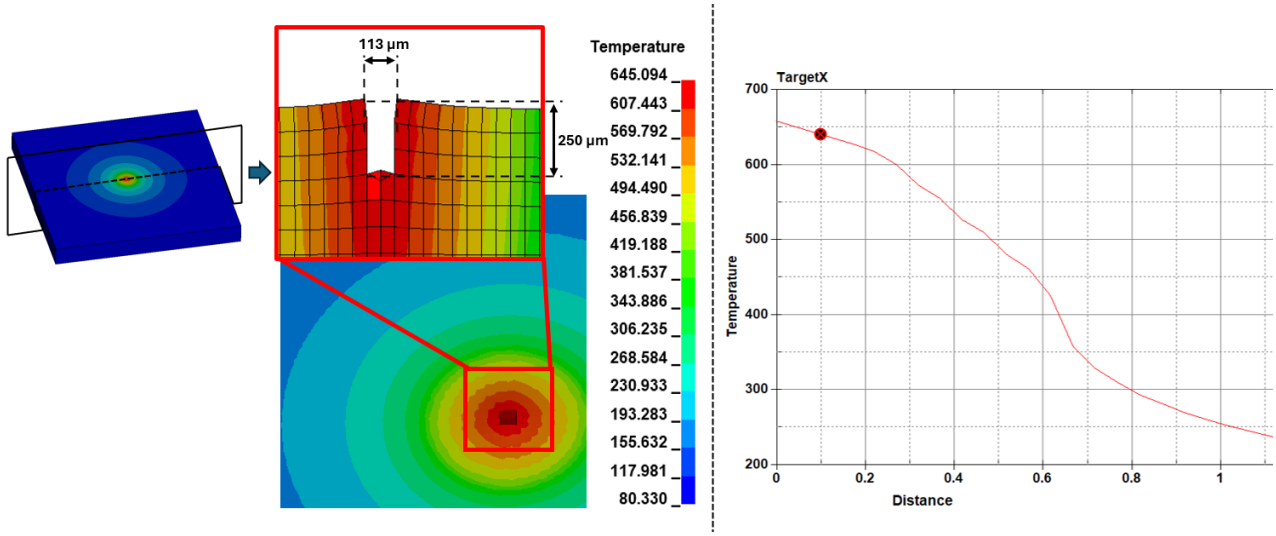


Figure 4.7. Representative simulated thermal distribution results. The cross-section depth is 250 µm

Comparing the FEM results with the experimental results [24] in Figure 4.8, a simulated area of 113 µm wide fails, while an approximate marked diameter of 130 µm is experimentally observed, compared to a 250 µm copper wire. The percentage difference of this comparison is 13%.

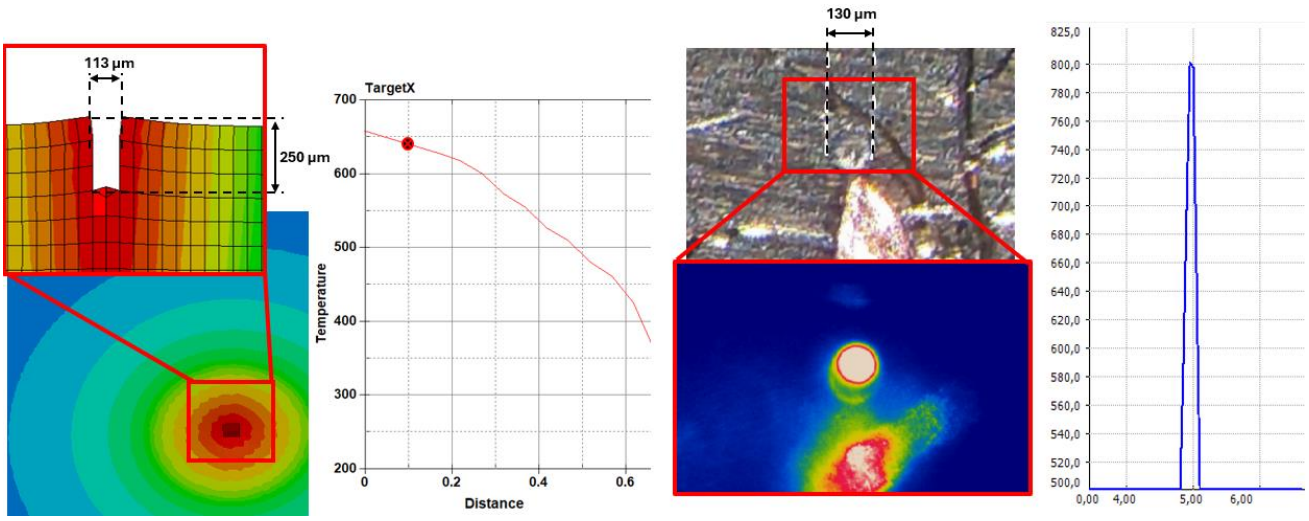


Figure 4.7. Representative results of simulation (left) and experiment (right)

The maximum computed FEM temperature for t = 68 ms was T = 706 °C, compared to the thermal camera maximum measured temperature, which for t = 100 ms was T = 736 °C (Figure 4.). Experimental limitations existed in the sampling time difference are due to the thermal camera recording at a frequency of f = 10 Hz or T = 100 ms, while the FEM simulation has a timestep of T = 5 ms or f = 200 Hz [24]. Since the experiment evolved in a millisecond scale, the FEM time step could not be increased, since we would lose accuracy in our simulation results.

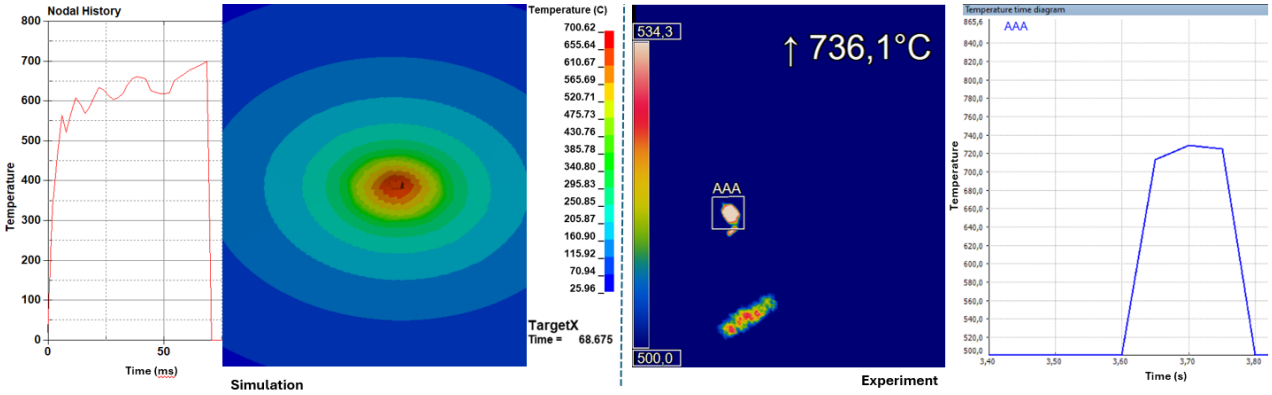


Figure 4.9. Thermal response representative simulation result (left) and experimental result (right)

At a given distance of 1 mm from the irradiated spot (Figure 4.8) the measured temperature was T = 195 °C, while the computed was T = 240 °C, (percentage difference 18.75%) for t = 200 ms.

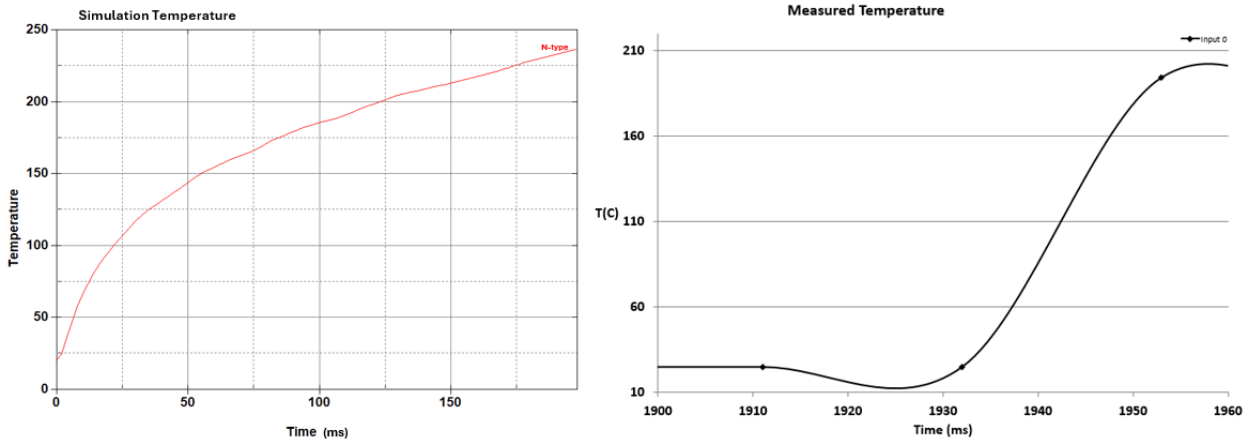


Figure 4.8. Simulation results of temperature (left), 1 mm from the center of the laser spot, compared to temperature measured by N-thermocouple (right).

Additional FEM simulations were carried out to model the laser-Al interaction using the same numerical parameters but with increased laser power of 400 W. The simulation results reveal a peak temperature of 708°C at 60 ms, immediately preceding material erosion. This process occurs more rapidly than in the 250 W case (erosion at 60 ms vs. 125 ms), with correspondingly faster temperature evolution and physical responses. Temperatures of 170 °C and 251 °C are computed for lateral distances of 2 mm and 1 mm from the irradiation center, respectively.

Figure 4.9 illustrates the simulated material response to a single laser pulse of 400 W power and 200 ms laser time duration. FEM model predicts the development of a thermal damage zone in the shape of a circular depression, equivalent to a hole diameter of around 214 µm. The temperature distribution is visualized through a contour plot, revealing a distinct thermal gradient radiating outward from the center of the irradiated zone.

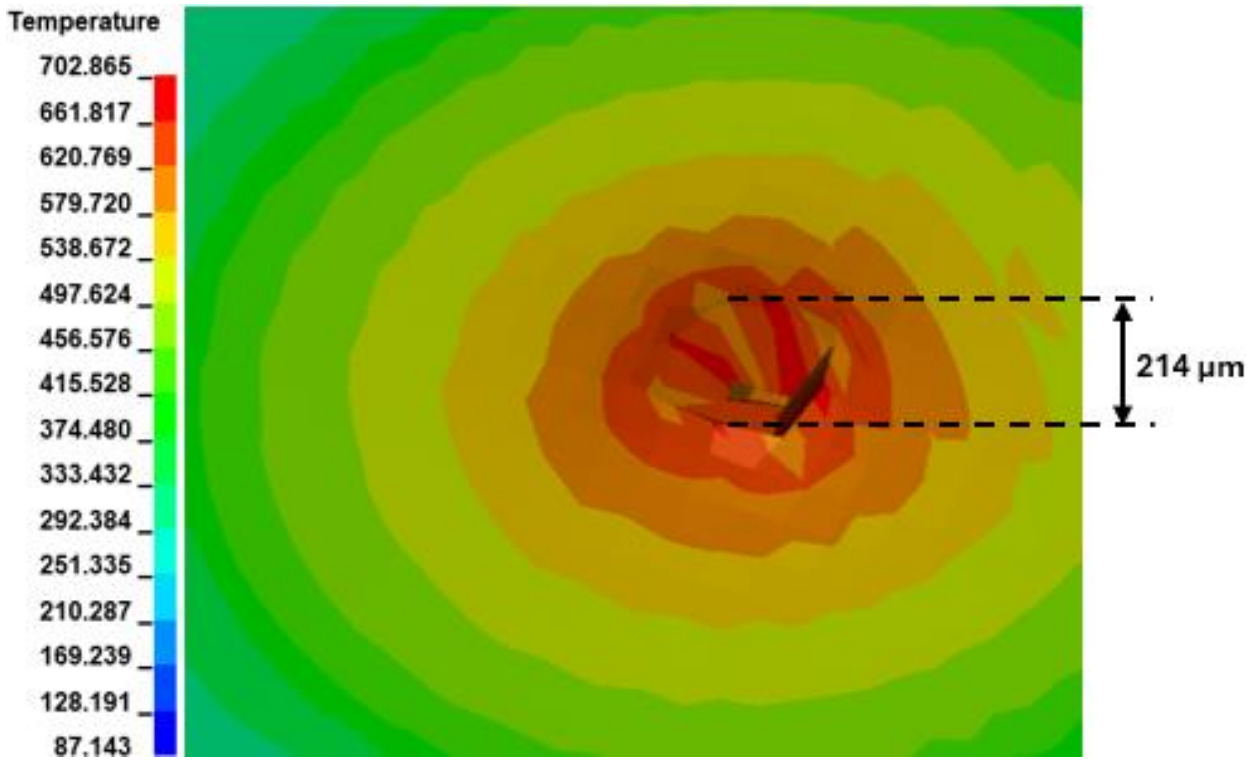


Figure 4.9. Contour plot of the representative simulation result at t = 200 ms

The material removal depth estimated by the FEM model is approximately 0.75 mm, much deeper than the 0.25 mm depth previously, because of the higher power (see Figure 4.12). The color map indicates the temperature distribution with the red region showing the utmost thermal and mechanical impact. The liquid phase is not explicitly simulated, as this would require a significantly more complex multiphysics model involving computational fluid dynamics (CFD) to simulate fluid flow, surface tension, and phase change effects. Yet for the purposes and intentions of this study, directed toward comprehending and foreseeing outcomes such as engraving, cutting, and plastic deformation, omitting the molten state is an acceptable simplification.

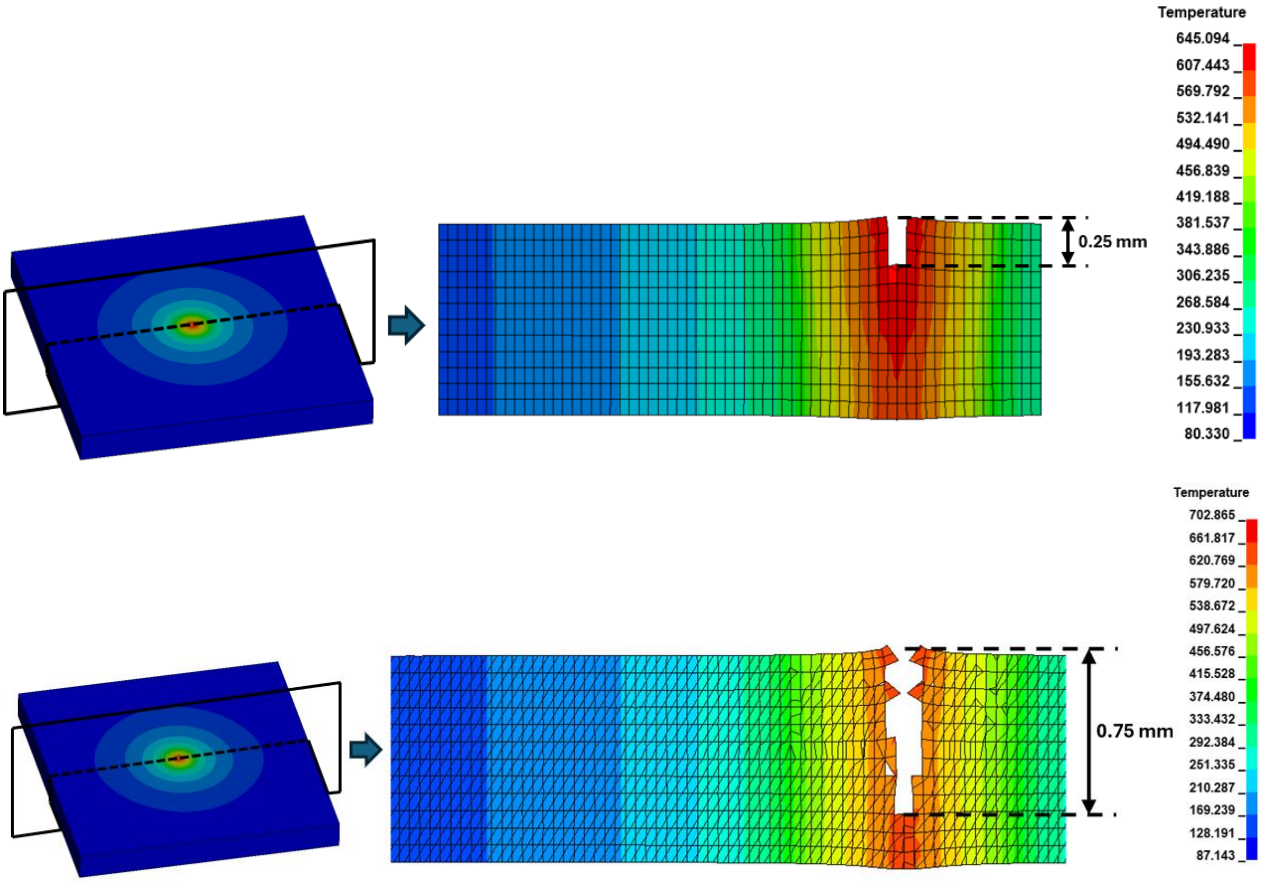


Figure 4.10. Simulated cross-section depth for 250 W (top) and 400 W (bottom) for t=200ms.

The temperature distribution (left, Figure 4.11) and the corresponding temperature history versus time (right, Figure 4.11) during laser irradiation is illustrated. The contour plot reveals the peak surface temperature of more than 700 °C at the center of the spot, with a monotonically decreasing radial profile. The time-temperature curve confirms a rapid initial spike followed by gradual build-up, approaching 260 °C at 200 ms.

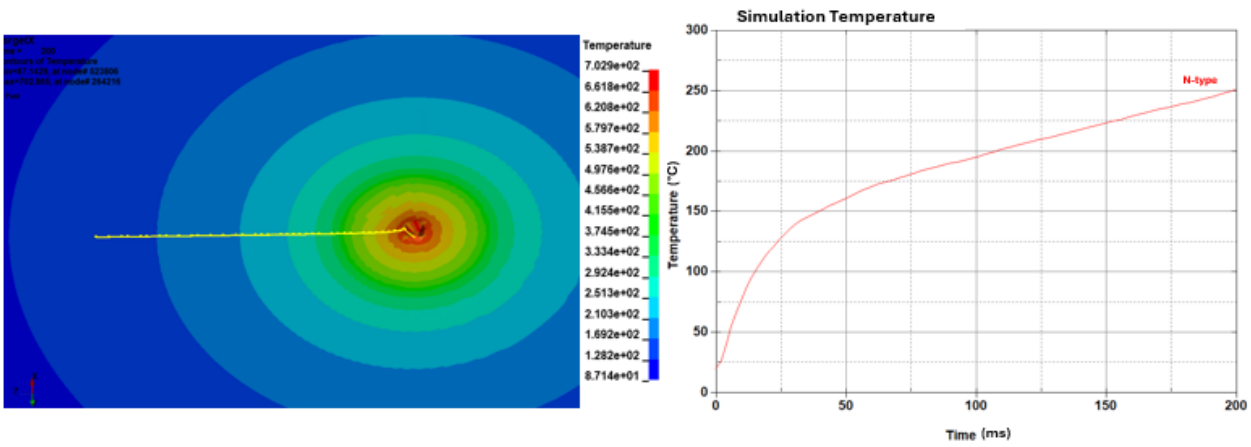


Figure 4.11. Temperature distribution (left) and simulated temperature vs time graph at a given distance of 1 mm from the irradiation spot

The corresponding experiment is performed using an N-type thermocouple [24]. The experimental results demonstrated that the thermal response of Al 1050 under the specified conditions aligns with the FEM results. The percentage difference, at 1 mm from the center of the laser spot, of the simulated and measured temperature by the N-Type thermocouple is 8.7%, as shown in Figure 4.12 below.

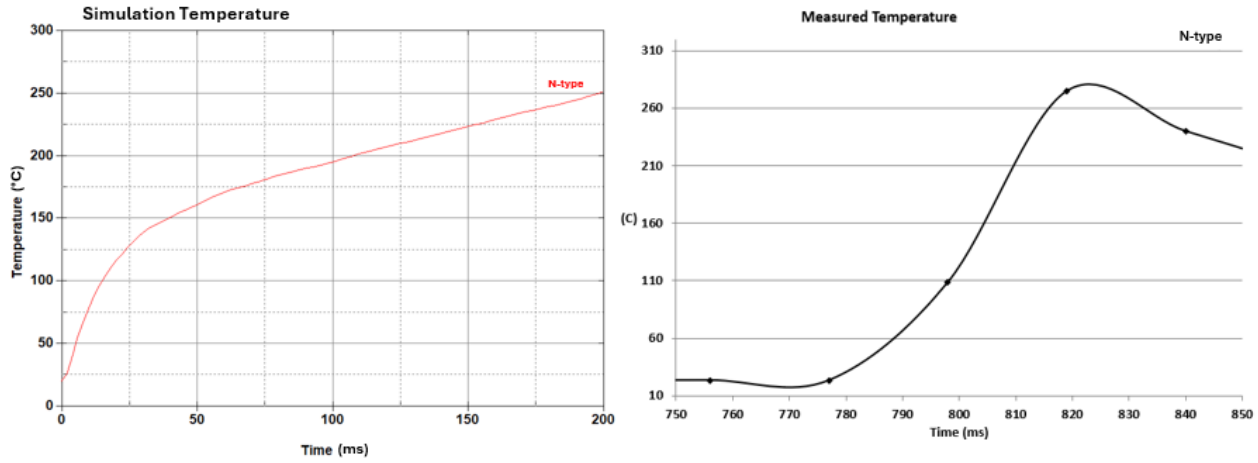


Figure 4.12. Simulation result of temperature (left), 1 mm from the center of the laser spot, compared to temperature measured by thermocouple (right)

Furthermore, thermal camera experimental measurements [24], show a maximum temperature of 1155 °C (Figure 4.13). The simulation maximum temperature occurs at 700 °C (Figure 4.13) since elements were removed due to damage criteria.

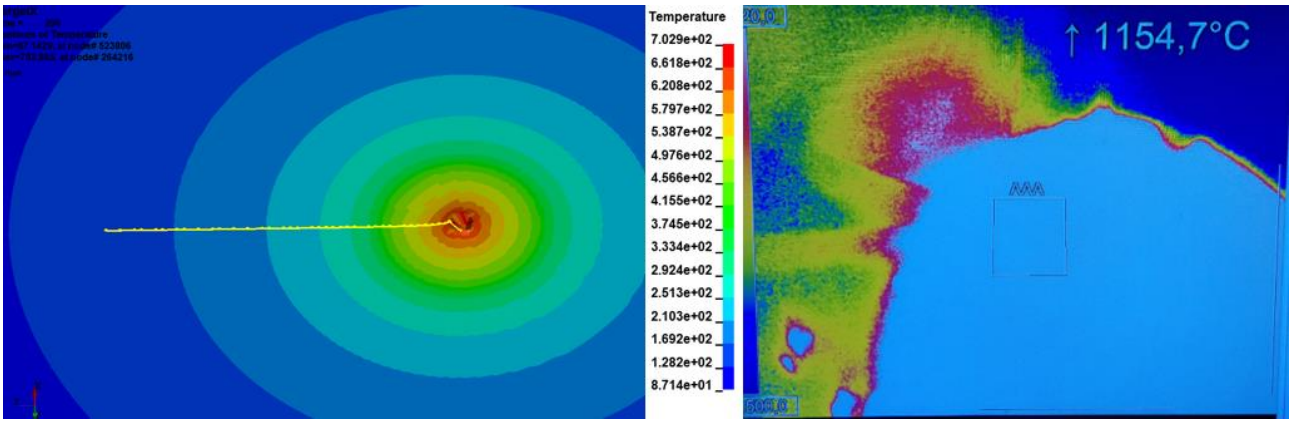


Figure 4.13. Thermal camera measured temperature result (right) compared to corresponding simulation result (left)

For the engraved spot, an approximate diameter measurement of 200 µm, compared to a reference 250 µm pure copper wire, is experimentally identified, agreeing well with the simulated result of 214 µm as presented in Figure 4.

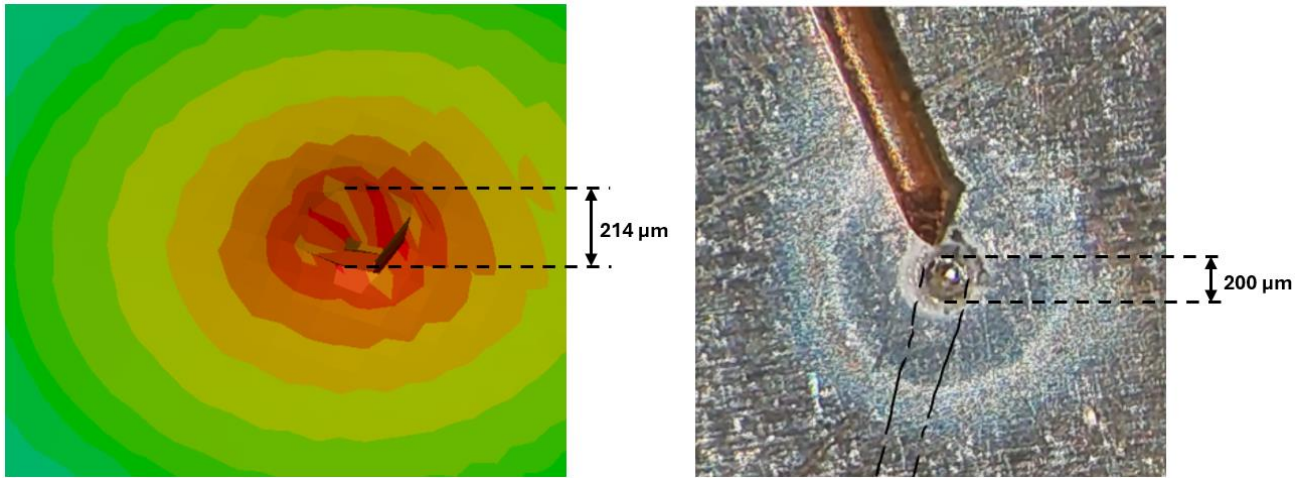


Figure 4.16. A representative simulation result compared to experimental result

The good agreement of the simulation results vs the experimental measurements secure the capability of the developed FEM model to simulate the transient dynamics of CW laser, Al sheet interactions in laser marking and engraving.

4.3 Laser linear marking

In laser marking, thermal stresses induced by the laser cause plastic deformation of the metal without melting or removing material. Instead, it results in localized heating that leads to a color change due to oxidation. This color change is typically a surface effect caused by controlled oxidation [20].

A 200 W continuous-wave laser beam is simulated to move along the +X axis with a length of 10 mm at a speed of 1200 mm/min on a 10 × 6 × 1 mm workpiece. The simulation is performed for simulation time 500 ms on HPC-ARIS in ambient air conditions. Average laser absorptivity of 32%, as experimentally found [24], is used. The simulated results are used in the experimental measurements from [24], while the numerical mesh and parameters/conditions follow the previous cases.

Figure 4. illustrates the simulated temperature distribution and plastic strain distribution. The maximum temperature is approximately 597 °C. The quasi-elliptical shape of the thermal zone may be due to anisotropic heat conduction or an inhomogeneous laser footprint. A plot of the effective plastic strain contour is also shown. The deformation field consists of a symmetrical, bi-lobed contour of up to 0.023 maximum strain. Strain localization is a sign of directional material flow or residual stress development due to thermal loading and material constraint interaction.

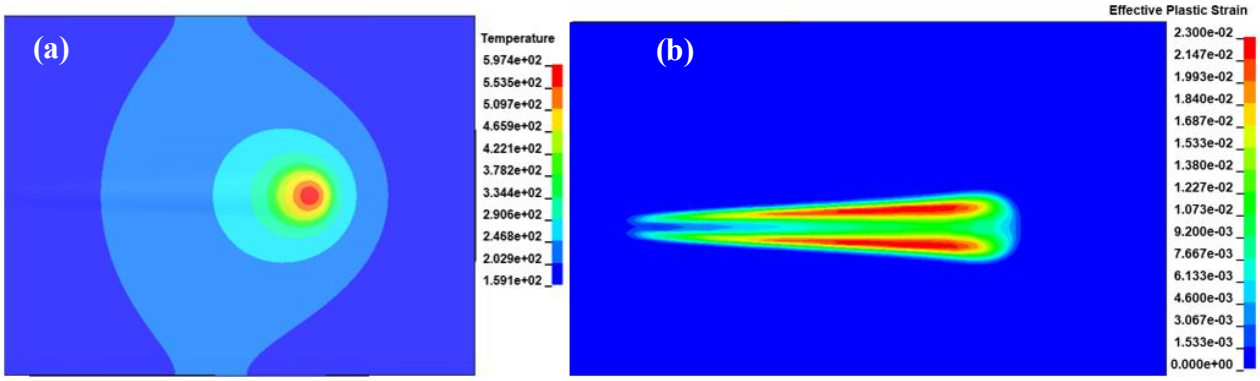


Figure 4.17. Thermal and Mechanical Simulation Results: Temperature Distribution and Plastic Strain

The FEM simulation results revealed a maximum temperature of approximately 600 °C during laser irradiation. During the experiment, the thermal camera recorded a maximum temperature of 600 °C in accordance with the computational results, below the melting point of the solid Al, as presented in Figure 4.. The two thermocouples measured a maximum temperature of 45 °C at 15 ms after laser irradiation, at 1 mm far from the center of the laser irradiation area. This measurement agreed well with the corresponding computed temperature.

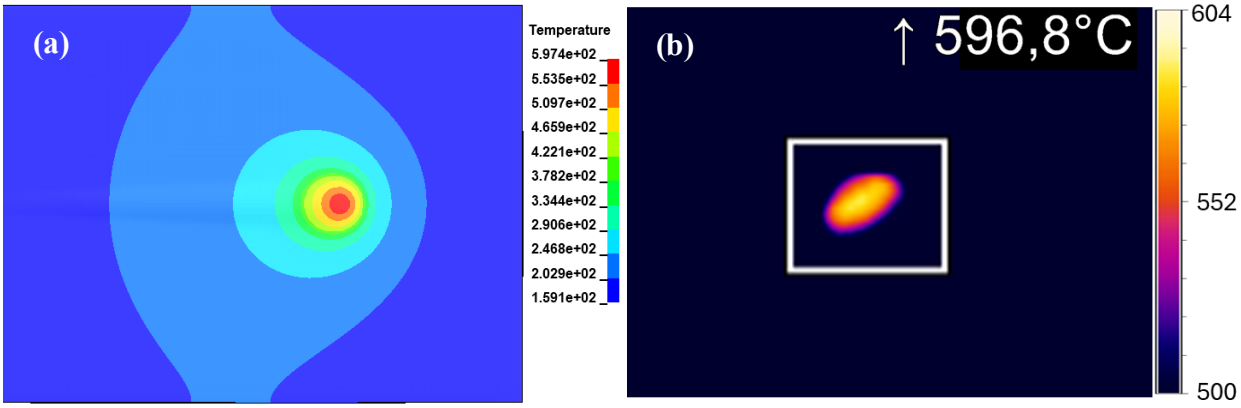


Figure 4.18. The simulated (left) and the experimentally measured temperature distribution (right)

The computed plastic deformation approached a maximum value of 0.023 for the effective plastic strain, on the Al samples surface, as shown in Figure 4. (a). Figure 4. (b) depicts a stereomicroscopy image of the machined Al surface, measured after the end of the experiment. Additionally, the WLI measurements depicted in Figure 4. (c-d), revealed a normal displacement of 0.25 μm on the Al surface.

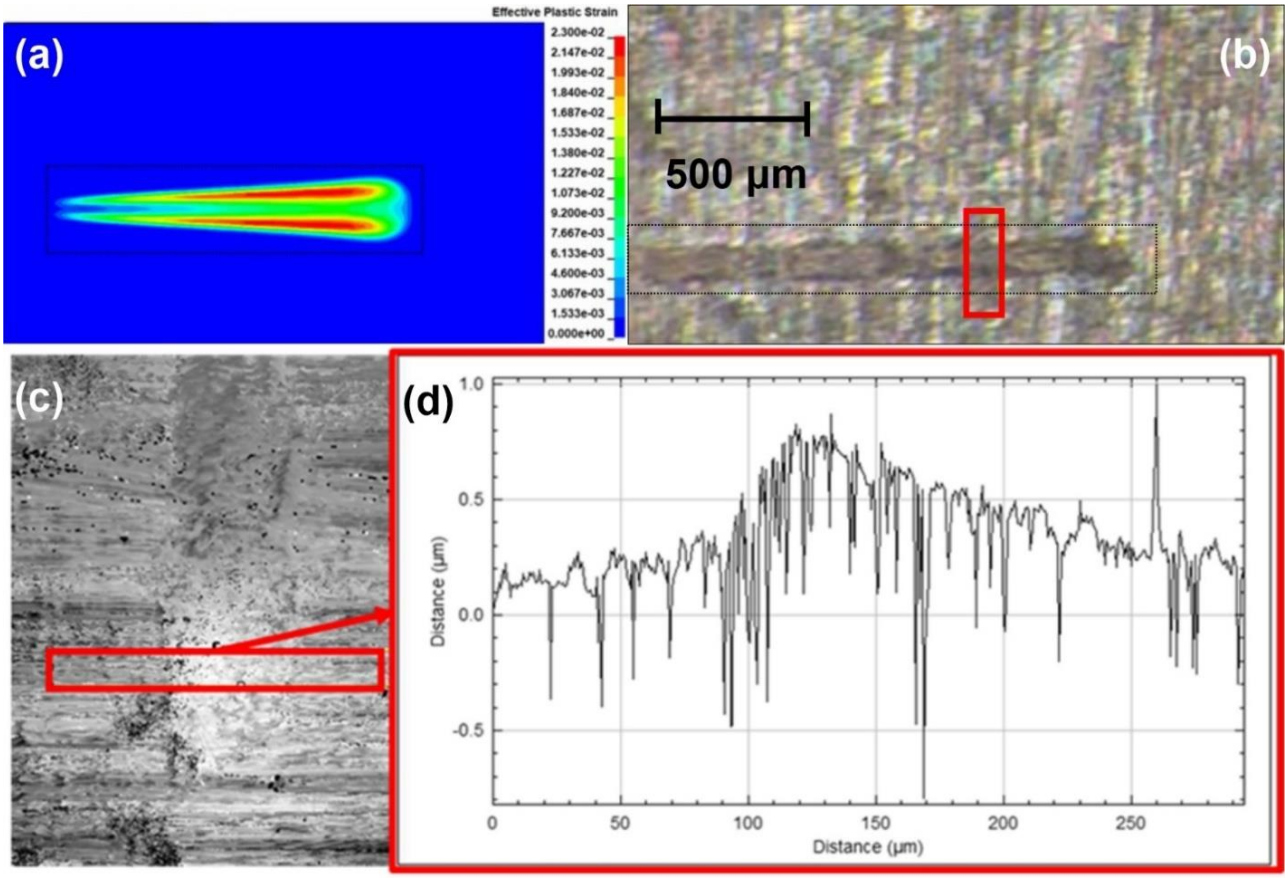


Figure 4.19. Simulated plastic strain (a) and a stereomicroscopic image of the linear marking (b). WLI measurement of the normal displacement (c, d). The red outlined rectangles indicate the area of measurement

4.4 Laser linear etching/engraving

During etching/engraving, the laser induces thermal stresses that result in plastic deformation of the metal and involves melting and material removal. Etching occurs when material is removed by less than 25 µm [25]. The objective is to simulate thermal responses and material ablation along the linear scan path for subsequent comparison with experimental observations.

A 200 W CW laser beam is simulated to move along the +X axis with a length of 10 mm at a speed of 75 mm/min on a 10 × 6 × 1 mm workpiece. The simulation is performed for 500 ms on HPC-ARIS in ambient air. Average laser absorptivity of 32% [24] is used. The simulated results are used in the experimental measurements from [24], while the numerical mesh and parameters are like the previous cases.

Figure 4.20 demonstrates results of laser etching for both experiment and simulation. There is a clear linear heat-affected zone visible at the surface and in accordance with the laser path. The simulated temperature ranges from ~163 °C (blue) to ~660 °C (red).

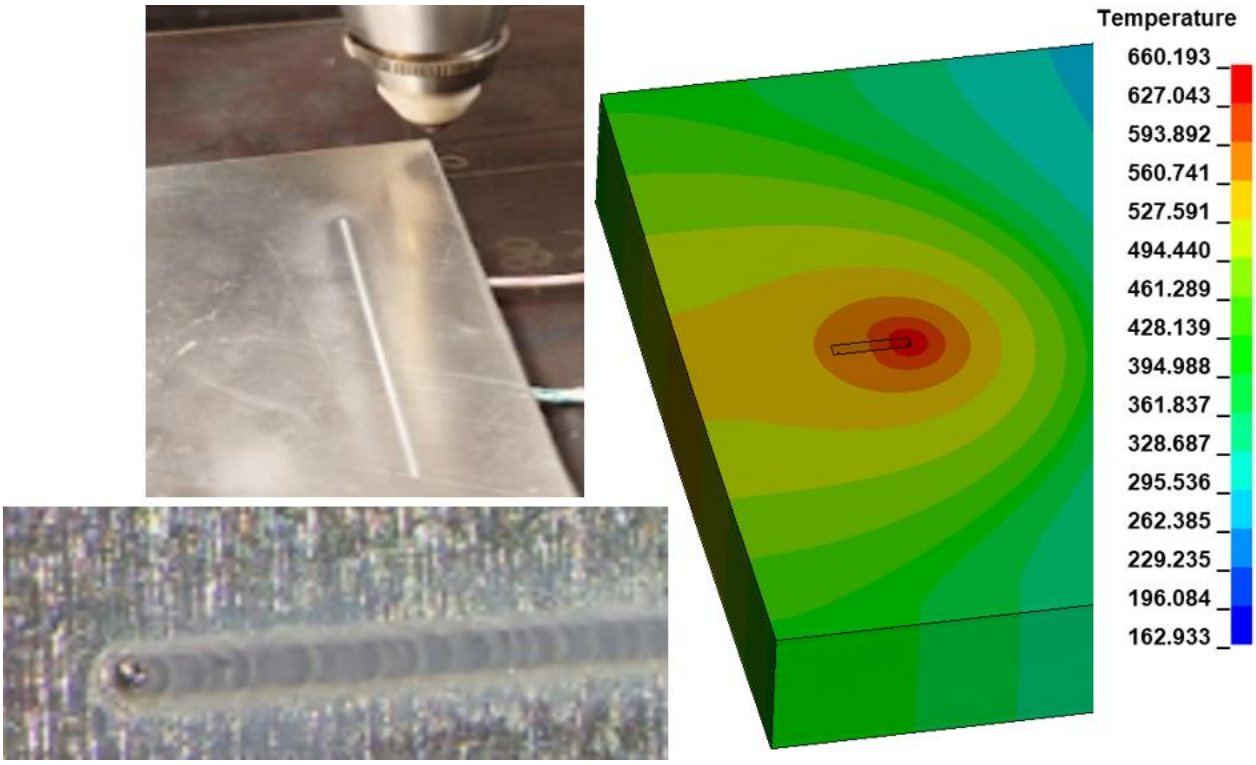


Figure 4.14. Laser etching and experimental stereoscopic view (left) and FEM temperature distribution 500 ms after the start of laser irradiation (right)

Retrieving the experimental results [24] utilizing a white light interferometer to measure the depth and width of the slot, we determined that it has a maximum depth of 10 µm and a width of 250 µm. A representative experimental result is shown in Figure 4.15. Corresponding simulation results, shown in Figure 4.14 computed the same width but at a depth of 20 µm.

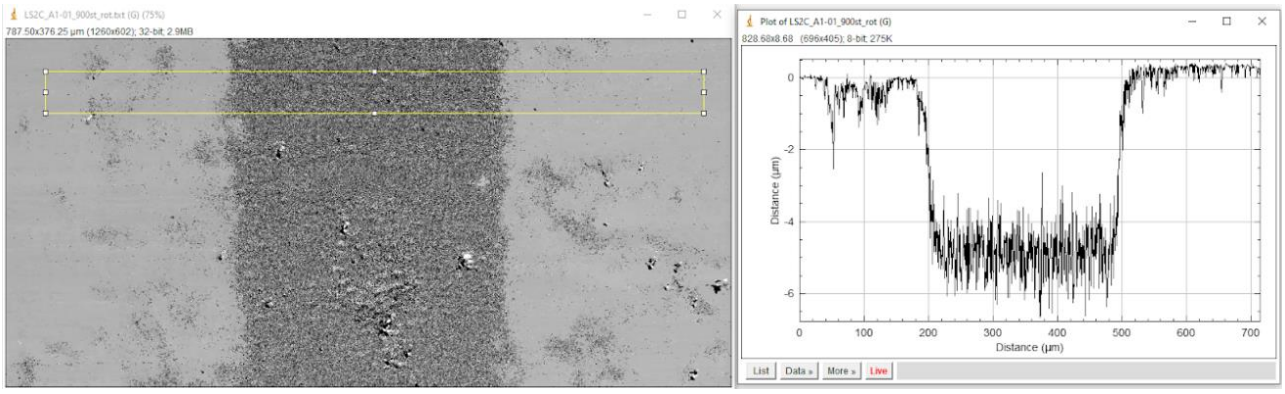


Figure 4.15. White light interferometry result retrieved from the experiments [24]

Figure 4.16 demonstrates the results of measured and computed temperature at 2 mm from the center of the laser irradiated spot. The thermocouple of K type placed at this distance measured a maximum temperature of 220 °C, while a maximum temperature of 210 °C is computed by the FEM simulation for the same distance 500 ms after the start of laser irradiation.

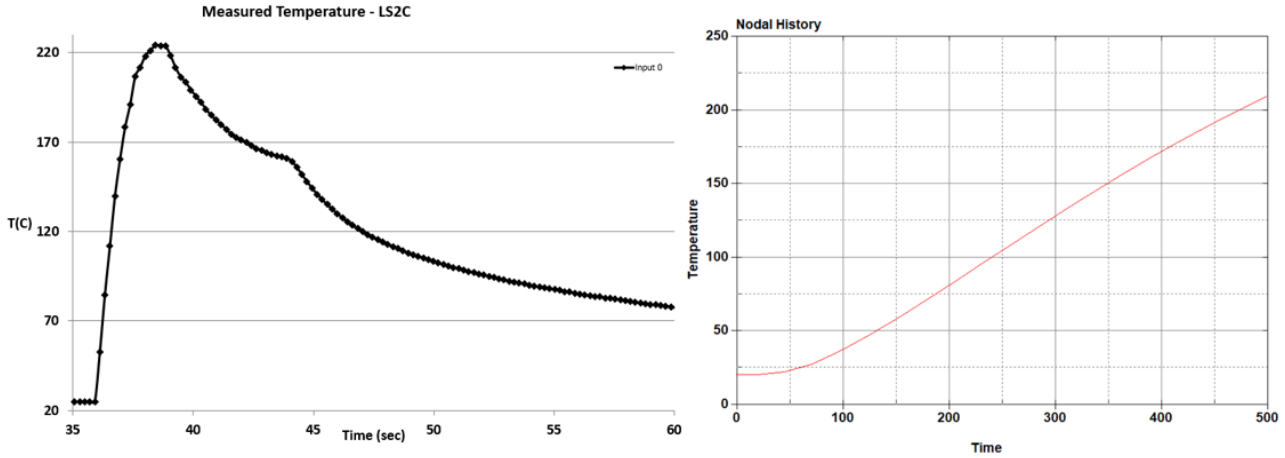


Figure 4.16. Measured temperature from the K-type thermocouple versus time (left) and the simulated temperature versus time (right) at a distance 2 mm away from the laser center

4.5 Laser linear cutting

Linear laser cutting is modeled and simulated, aiming to replicate material separation along a predefined path. The model captures thermal gradients, stress accumulation, and melting behavior to predict effective cutting performance under controlled laser parameters.

A 450 W CW laser beam is simulated to move along the +X axis with a length of 10 mm at a speed of 60 mm/min on a $10 \times 6 \times 1$ mm workpiece. The simulation is performed for simulation time 500 ms on HPC-ARIS in ambient air conditions. Average laser absorptivity of 32%, as experimentally found [24], is used. The simulated results are used in the experimental measurements from [24], while the numerical mesh and parameters/conditions are like the previous cases.

Figure 4.23 demonstrates a close-up result of a FEM simulation of the laser cutting process. On the left an expanded, cross-sectional view of the material after the laser exposure is shown. It distinctly outlines a well-defined internal channel or kerf, that indicates where the material is laser cut. The cut width is measured to be 305 μm. The surrounding material is presented in the form of a heatmap, giving the temperature profile surrounding the cut. Red and orange regions indicate higher temperatures, which represent the high thermal energy delivered by the 450 W laser. On the right the temperature vs. time plot is depicted. The graph is the thermal evolution curve at a single node in the simulated material, 1 mm from the interaction zone of the laser. The graph shows a slow increase in temperature over time, slowly rising to approximately 200 °C near the end of the 500 ms. This slow rise in temperature at the measurement location conveys the continuous input of thermal energy supplied by the 450 W laser, which is critical to maintain the material removal process in laser cutting.

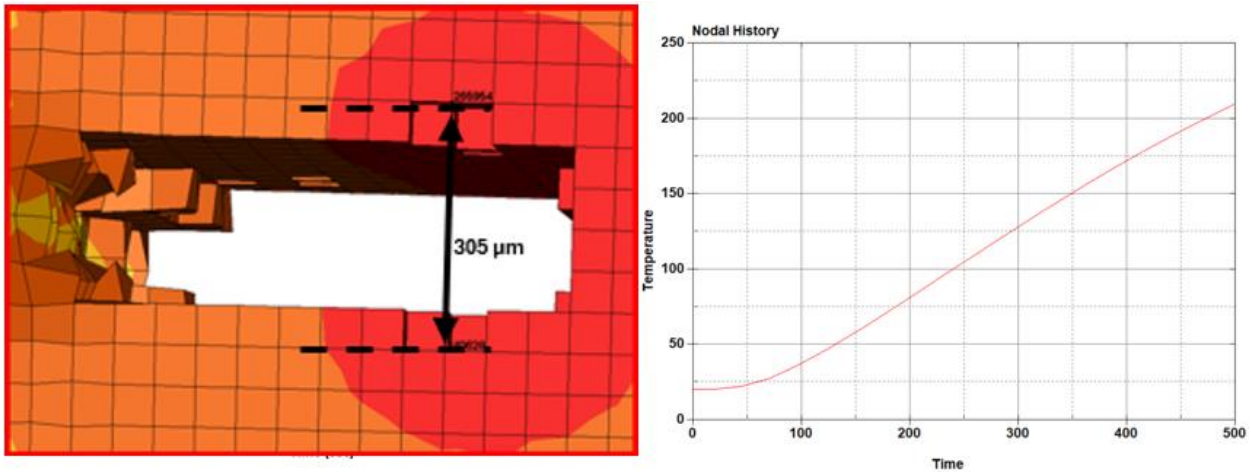


Figure 4.23. Simulated material removal and thermal evolution in laser cutting

Figure 4.17 presents also representative results from the laser cutting case study compared to WLI experimental results [24].

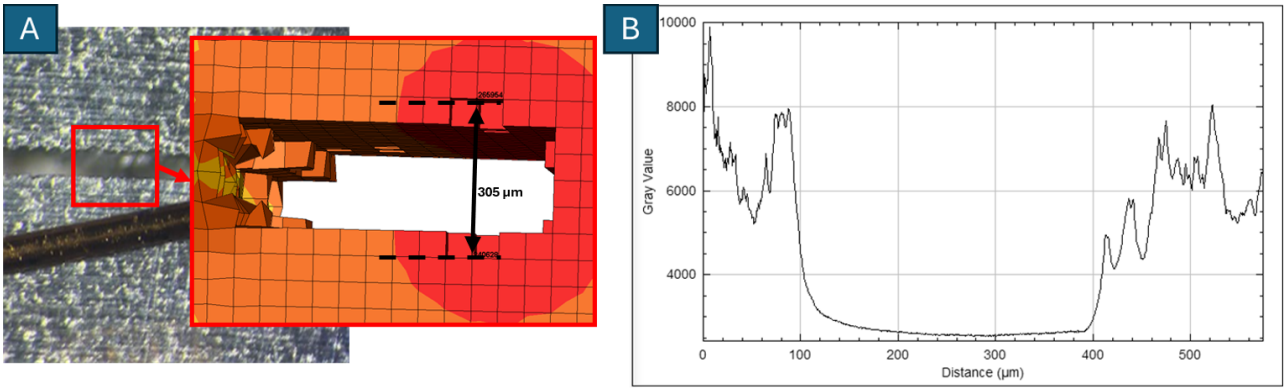


Figure 4.17. a) Image of the cut area from the stereoscope alongside the corresponding FEM simulation result, b) Graph from WLI indicating an approximate cutting width of 300 µm

5. Conclusions

In this thesis, laser-material interactions were investigated through FEM simulations of aluminum alloy Al 1050. The research encompassed laser cutting, engraving/etching, marking, and plastic deformation processes, each offering critical insights into the relationship between laser parameters and material behavior. Both single-pulse and continuous laser motions, were explored on workpieces of various thicknesses (0.6 mm, 1 mm, 2 mm, and 3 mm), enabling broader insight into the thermomechanical responses under varying machining conditions. The simulated thermal and mechanical responses showed strong agreement with experimental measurements.

Material absorptivity plays a significant role in both experimental results and the accuracy in simulation. Variations in absorptivity, driven by factors such as temperature, surface roughness, cleanliness, surface oxidation during engraving and the transition of the material to a liquid state are among the factors that alter absorptivity, introducing variability in experimental conditions. These fluctuations directly influenced the reliability of the FEM simulation predictions. Despite these, a reasonable mean percentage difference of about 15% is obtained between the simulated and experimental results. Importantly, we found that the highest accuracy of the simulations was achieved under well-controlled experimental conditions with minimal variations in absorptivity.

The significance of air assistance in laser cutting was also stressed, especially in high-power processing, as it played a great role in molten material ejection, oxidation reduction, and enhancement of cutting quality. Optimizing micromachining parameters—piercing delay time, scan speed, and back splatter suppression—was also stressed in the study to enhance cut quality and minimize defects like dross.

In general, the research not only demonstrated the validity of FEM simulations as a tool for understanding laser-material interaction processes but also identified key areas for further development. In addition, the research demonstrates that by controlling the continuous wave (CW) laser parameters power, pulse duration, and scanning speed, precise control of material response can be achieved to create more efficient and reliable industrial laser machining processes. The contributions of this work will expand the knowledge base for developing predictive modeling techniques in laser manufacturing processes and optimizing their industrial applications. Further work is needed to study the failure criteria of the FEM model to accurately simulate the effects of laser cutting.

Appendix – Laboratory Equipment

In this chapter, we present all the laboratory equipment, explaining the role, function, and specifications of each element in the laser machining setup. The major tools described include a lathe machine, a CW high-power fiber laser, a 3-axis CNC milling machine, and various hand tools that played a crucial role in conducting controlled laser-metal experiments on aluminum (Al) samples. The integration of the laser equipment with the CNC machine is detailed, including mounting solutions and alignment techniques. Additionally, the software communication setup is explained, where Mach3 and Trumpf Fiberview software are configured for synchronized control. This configuration enables precise coordination between CNC movements and laser activation, ensuring optimal machining results.

Appendix A - Lathe

A lathe is a general-purpose machine tool most used for operations in which the workpiece is rotated while a cutting tool is pressed against it. This configuration makes the lathe highly effective for fabricating symmetric objects with high precision. For this reason, it is essential for producing parts such as cylindrical shafts, bolts, and other components requiring uniform diameters and smooth surfaces. Lathe operations include turning, which reduces the diameter of the workpiece; facing, which smooths the ends; as well as drilling, threading, and knurling. Various types of lathes are available, including engine lathes, turret lathes, and CNC lathes, each designed for different levels of complexity and production requirements. While conventional lathes are manually operated, modern CNC lathes allow for automated and programmable operations, enabling repeatable precision on complex parts.

In our laboratory, we use the Hungarian SZERSZÁMGÉPIPARI MŰVEK Lathe (Figure 5.1), a highly accurate machine capable of performing both simple and complex turning tasks. The machine is equipped with a 2.2 kW spindle motor, enabling it to achieve high rotation speeds of up to 2500 RPM. It features a swing diameter of 222 mm and a maximum turning length of 1500 mm, making it versatile for a wide range of materials and part sizes. Additionally, the lathe is built with a rigid frame structure that ensures excellent dimensional accuracy and surface finish, both of which are critical for producing high-quality components.



Figure 5.1. Hungarian SZERSZAMGEPIPARI MUVEK Lathe machine

Additionally, for future experiments, we have modified the existing lathe in IPPL to serve as a tool for Laser-Assisted Machining (LAM) [21] processes. A Digital Readout (DRO) has been added to the lathe, allowing precise, real-time tracking of the cutting tool's position. The DRO improves control by displaying exact measurements, thereby enhancing the accuracy and consistency of cuts. Furthermore, we mounted the PIPAQ "PQRU-S" Flange Mounted laser collimator onto the lathe. Using a custom monitor arm, the collimator was positioned vertically above the workpiece to ensure precise laser alignment during processing. This setup significantly enhances the precision of the machining system (Figure 5.2), enabling controlled and highly accurate material shaping to meet experimental requirements.

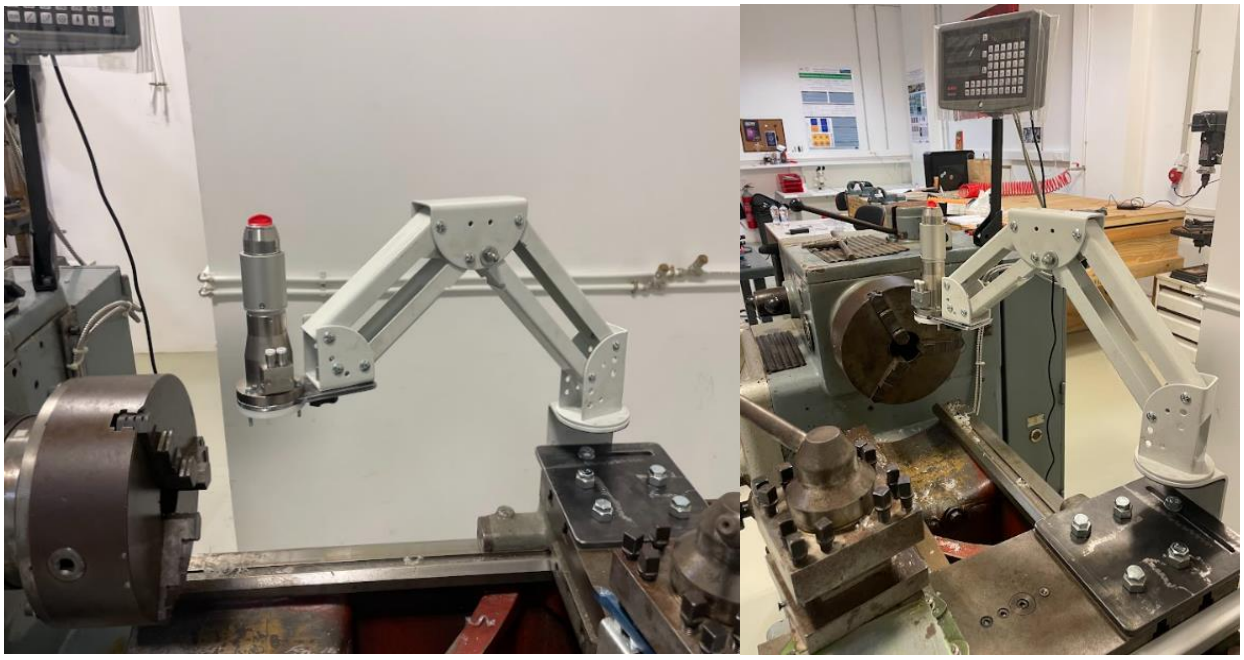


Figure 5.2. Lathe machine modified for LAM processes, to hold a collimator (left) vertically to the work area with a DRO (right) to enhance control and precision

Appendix B - 3 axis CNC

The 3-axis CNC milling machine is a highly precise tool capable of automated material shaping across multiple axes, making it ideal for manufacturing complex components with exceptional accuracy. These machines operate along three perpendicular axes: X, Y, and Z, allowing the cutting tool to move simultaneously across multiple axes. This capability makes them highly versatile, enabling operations such as drilling, milling, and cutting with flexibility and repeatability during the manufacturing process. The machine is controlled by a computer program that defines the tool paths, allowing it to consistently reproduce complex geometries with close tolerances.

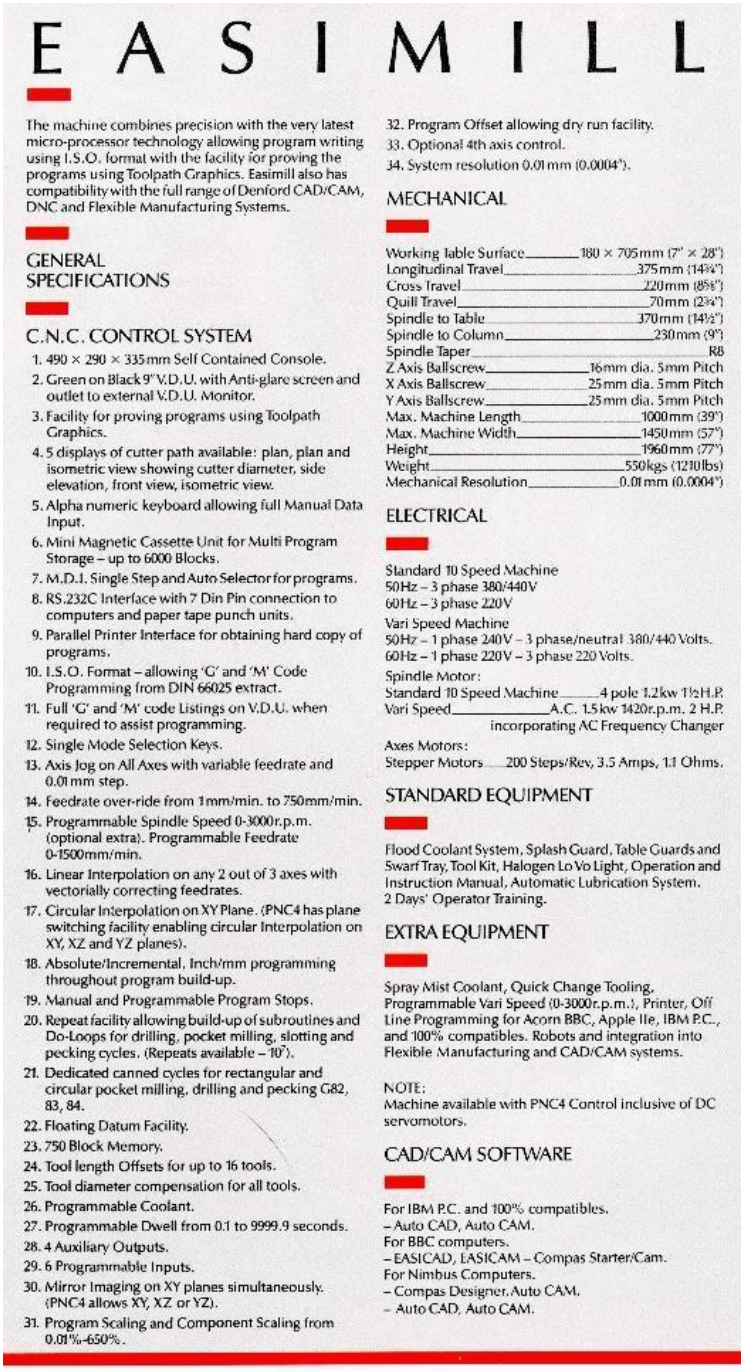
Our laboratory is equipped with a Denford EASIMILL 3 Vertical Turret CNC (Figure 5.3), which was later adapted to carry a laser cutting head for conducting all laser machining experiments.



Figure 5.3. Denford Easimill 3 CNC machine

The CNC is equipped with a 1.5 kW spindle motor and three stepper motors that control movements along the X, Y, and Z axes. These stepper motors perform 200 steps per revolution and provide a work area with motion limits of 378 mm on the X-axis, 180 mm on the Y-axis, and 80 mm on the Z-axis. This setup offers a practical workspace capable of handling mid-sized experimental samples. The system resolution is up to 0.01 mm, and the maximum feed rate achievable by the stepper motors is 1500 mm/min (Figure 5.4). This flexibility allows a wide range of speeds suitable for different machining operations: slower speeds ensure greater control and accuracy for delicate or complex cuts, while faster speeds optimize efficiency for less intricate operations. Each stepper motor is connected to its own motor driver, which reads signals from the CNC controller to regulate the motor's steps and direction with high precision. This design ensures smooth and coordinated motion across all three axes, a critical factor in maintaining consistent quality during laser machining operations. The CNC controller signals define the number of steps and the direction each motor must take, allowing the tool to be positioned with precision at any

moment. This granular control is essential in our experimental setup, where precise laser positioning is required to ensure uniform energy application and consistent material processing.



EASIMILL

The machine combines precision with the very latest micro-processor technology allowing program writing using I.S.O. format with the facility for proving the programs using Toolpath Graphics. Easimill also has compatibility with the full range of Denford CAD/CAM, DNC and Flexible Manufacturing Systems.

GENERAL SPECIFICATIONS

C.N.C. CONTROL SYSTEM

1. 490 × 290 × 335mm Self Contained Console.
2. Green on Black 9" V.D.U. with Anti-glare screen and outlet to external V.D.U. Monitor.
3. Facility for proving programs using Toolpath Graphics.
4. 5 displays of cutter path available: plan, plan and isometric view showing cutter diameter, side elevation, front view, isometric view.
5. Alpha numeric keyboard allowing full Manual Data Input.
6. Mini Magnetic Cassette Unit for Multi Program Storage – up to 6000 Blocks.
7. M.D.I. Single Step and Auto Selector for programs.
8. RS.232C Interface with 7 Din Pin connection to computers and paper tape punch units.
9. Parallel Printer Interface for obtaining hard copy of programs.
10. I.S.O. Format – allowing 'G' and 'M' Code Programming from DIN 66025 extract.
11. Full 'G' and 'M' code Listings on V.D.U. when required to assist programming.
12. Single Mode Selection Keys.
13. Axis Jog on All Axes with variable feedrate and 0.01 mm step.
14. Feedrate over-ride from 1mm/min. to 750mm/min.
15. Programmable Spindle Speed 0-3000r.p.m. (optional extra). Programmable Feedrate 0-1500mm/min.
16. Linear Interpolation on any 2 out of 3 axes with vectorially correcting feedrates.
17. Circular Interpolation on XY Plane. (PNC4 has plane switching facility enabling circular Interpolation on XY, XZ and YZ planes).
18. Absolute/Incremental, Inch/mm programming throughout program build-up.
19. Manual and Programmable Program Stops.
20. Repeat facility allowing build-up of subroutines and Do-Loops for drilling, pocket milling, slotting and pecking cycles. (Repeats available – 10).
21. Dedicated canned cycles for rectangular and circular pocket milling, drilling and pecking G82, 83, 84.
22. Floating Datum Facility.
23. 750 Block Memory.
24. Tool length Offsets for up to 16 tools.
25. Tool diameter compensation for all tools.
26. Programmable Coolant.
27. Programmable Dwell from 0.1 to 9999.9 seconds.
28. 4 Auxiliary Outputs.
29. 6 Programmable Inputs.
30. Mirror Imaging on XY planes simultaneously. (PNC4 allows XY, XZ or YZ).
31. Program Scaling and Component Scaling from 0.01%-650%.
32. Program Offset allowing dry run facility.
33. Optional 4th axis control.
34. System resolution 0.01 mm (0.0004").

MECHANICAL

Working Table Surface	180 × 705mm (7" × 28")
Longitudinal Travel	375mm (14¾")
Cross Travel	220mm (8⅝")
Quill Travel	70mm (2¾")
Spindle to Table	370mm (14½")
Spindle to Column	230mm (9")
Spindle Taper	R8
Z Axis Ballscrew	16mm dia. 5mm Pitch
X Axis Ballscrew	25mm dia. 5mm Pitch
Y Axis Ballscrew	25mm dia. 5mm Pitch
Max. Machine Length	1000mm (39")
Max. Machine Width	1450mm (57")
Height	1960mm (77")
Weight	550kgs (1210lbs)
Mechanical Resolution	0.01mm (0.0004")

ELECTRICAL

Standard 10 Speed Machine
50Hz – 3 phase 380/440V
60Hz – 3 phase 220V

Vari Speed Machine
50Hz – 1 phase 240V – 3 phase/neutral 380/440 Volts.
60Hz – 1 phase 220V – 3 phase 220 Volts.

Spindle Motor:
Standard 10 Speed Machine — 4 pole 1.2kw 1½H.P.
Vari Speed — A.C. 1.5kw 1420r.p.m. 2 H.P. incorporating AC Frequency Changer

Axes Motors:
Stepper Motors — 200 Steps/Rev, 3.5 Amps, 1.1 Ohms.

STANDARD EQUIPMENT

Flood Coolant System, Splash Guard, Table Guards and Swarf Tray, Tool Kit, Halogen Lo Vo Light, Operation and Instruction Manual, Automatic Lubrication System. 2 Days' Operator Training.

EXTRA EQUIPMENT

Spray Mist Coolant, Quick Change Tooling, Programmable Vari Speed (0-3000r.p.m.), Printer, Off Line Programming for Acorn BBC, Apple IIe, IBM P.C., and 100% compatibles. Robots and integration into Flexible Manufacturing and CAD/CAM systems.

NOTE:
Machine available with PNC4 Control inclusive of DC servomotors.

CAD/CAM SOFTWARE

For IBM P.C. and 100% compatibles.
– Auto CAD, Auto CAM.
For BBC computers.
– EASICAD, EASICAM – Compas Starter/Cam.
For Nimbus Computers.
– Compas Designer, Auto CAM.
– Auto CAD, Auto CAM.

Figure 5.4. Denford's Easimill 3 CNC General Specifications table

Key to both the functionality and safety of the machine is the CNC controller interfaces. The principal elements involved are illustrated in Figure 5.5:

- 5 Digital Outputs: These outputs control CNC motion, enabling the precise coordination of axis movements according to programmed parameters.
- 6 Digital Inputs: Primarily safety features, the digital inputs act as emergency stop triggers. This setup ensures that in the event of an unplanned error or a manual stop command, the machine halts immediately, protecting both the equipment and the operator.
- Power Supply: A stable power supply supports the controller, drivers, and motors, providing consistent energy for reliable operation during long machining cycles.
- PC Control Interface: The CNC is interfaced with a PC running Mach3 software, which serves as the main control platform for managing and programming operations. This interface allows the operator to load machining code, adjust movement parameters, and monitor real-time performance.
- Digital Display: The CNC includes a digital display that shows the system status, movement coordinates, and other key metrics. This provides immediate visual feedback, aiding in setup and troubleshooting.

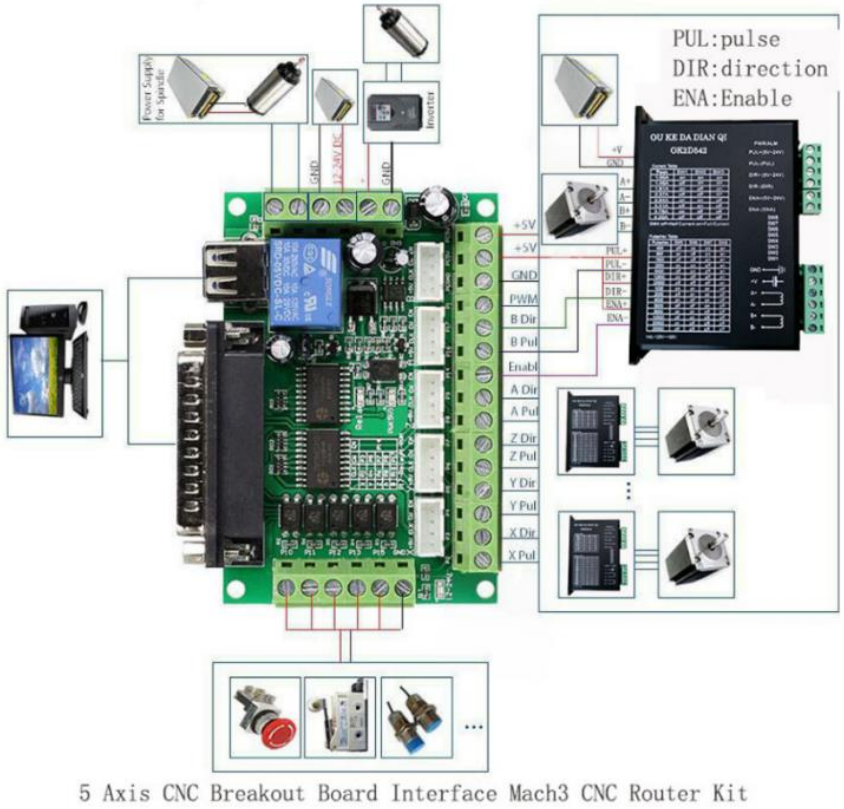


Figure 5.5. CNC Controller interfaces

Appendix C - CNC Software

Mach3 Software for CNC Control

Mach3 is the primary software used to drive the CNC machine. It is a popular and versatile CNC control software widely used in both industrial and experimental settings (Figure 5.6). Installed on the PC connected to the Denford EASIMILL 3 CNC, Mach3 serves as the main interface between the user/operator and the CNC hardware. This software enables full control and programming of the CNC's movements, allowing the operator to adjust machining parameters such as speed, feed rate, and movement paths.

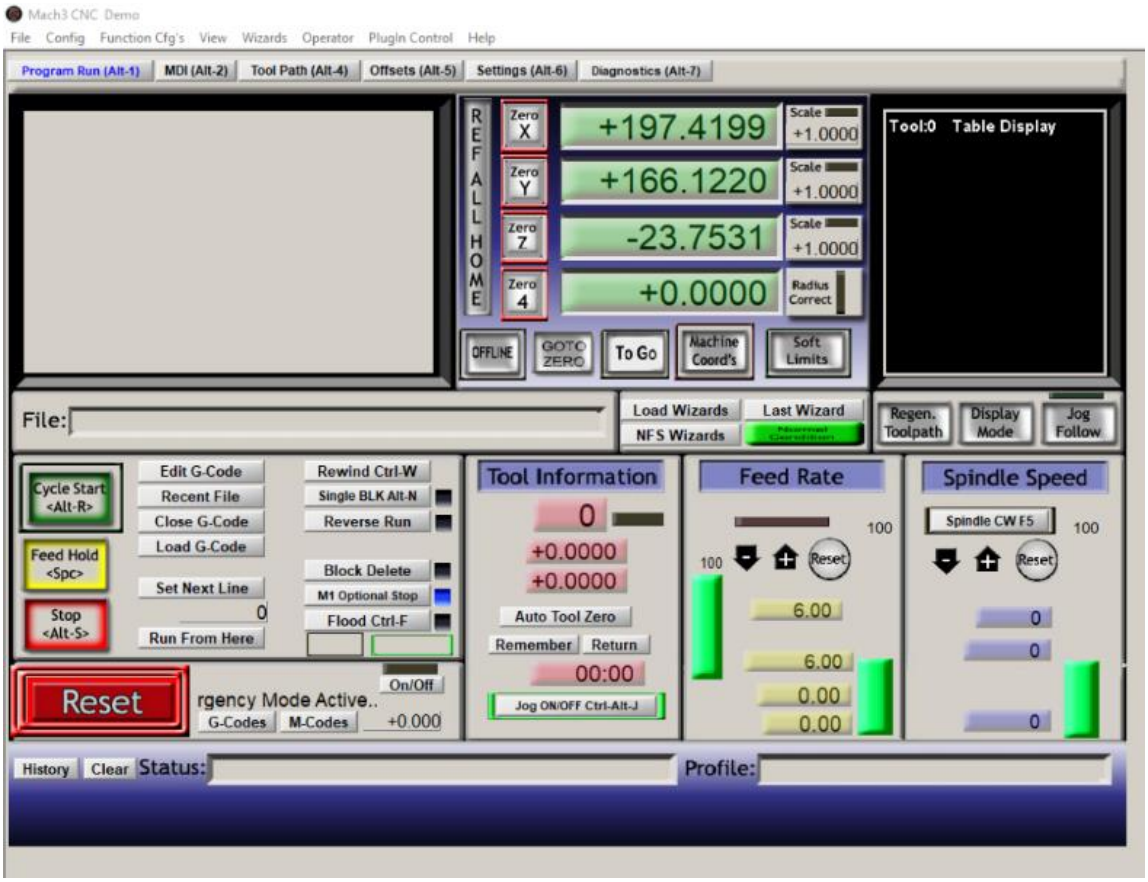


Figure 5.6. Artsoft's Mach3 interface

Mach3 interprets G-code into specific motor movements to control the CNC's motion along the three dimensions: X, Y, and Z. Additionally, the software allows for real-time monitoring and adjustment of the CNC's operation, providing information on position, velocity, and other critical metrics. In this thesis, Mach3's flexibility in supporting custom scripts and integrating the control

of both CNC and laser operations is particularly important, as it enables seamless coordination between the CNC and laser systems for synchronized operation.

Appendix D - High-power fiber laser

High-power fiber lasers are advanced laser platforms that use optical fibers doped with rare-earth elements to produce focused, high-intensity laser beams. With their efficiency, precision, and flexibility, these lasers are highly suitable for demanding industrial applications such as material cutting, welding, and processing. Compared to traditional laser sources, high-power fiber lasers offer several advantages, including improved beam quality, higher power output, and superior thermal management. Since they can deliver focused energy with minimal divergence, these lasers are widely utilized in industries such as aerospace, automotive, and manufacturing, where precision and speed are essential.

Laser Hardware

Laser module: Trumpf TruFiber P compact

The core component of the laser equipment, used in this thesis, is the Trumpf TruFiber P compact laser module (Figure 5.7). This CW fiber laser delivers up to 2000 W of power at a wavelength of 1.075 μm and is robust enough for advanced industrial applications. Featuring inherently high beam quality, the fiber laser design produces a narrow and highly concentrated beam, enabling precise material processing to the finest detail. This makes it well-suited for applications such as cutting, welding, and engraving on metallic surfaces.

In this thesis, the CW laser will be utilized for controlled laser machining on Al samples, leveraging its stability, consistent power delivery, and adaptability to various machining requirements. Its durable construction ensures uninterrupted operation, a critical feature for extended experimental measurements where precision and reliability are of utmost importance.



Figure 5.7. Trumpf's 2000 W High-power CW fiber laser

Laser cutting head: Precitec LightCutter 2.0 motorized 3D

The LightCutter 2.0 Motorized 3D (Figure 5.22) is a laser cutting head developed by Precitec for various metal treatment processes. It is specifically designed for use in fiber laser systems requiring high precision and process stability, such as laser cutting. The motorized feature of the LightCutter 2.0 allows for automatic adjustment of focal positions and other cutting parameters through motorized actuators, ensuring high-quality cuts across different material thicknesses.



Figure 5.8. Precitec LightCutter 2.0 motorized 3D laser cutting head

The advanced features of the LightCutter 2.0 are as follows:

- Automatic Focal Position Adjustment: Motorized adjustment enables high-quality cuts across different material thicknesses.
- Lasermatic Technology: A closed-loop monitoring system that optimizes the focal position automatically with exceptional accuracy, minimizing defects.
- CNC Integration: Seamlessly integrates with CNC systems for complex and precise cuts.
- Cooling System: Features air or liquid cooling to maintain optimal operating temperatures during continuous high-power operation.
- Sensing and Monitoring: Equipped with onboard sensors to detect lens contamination or misalignment.

Specifications include:

- Focal Length: 150 mm
- Focal Spot: 250 µm
- Maximum Cutting Gas Pressure: 25 bar

These features ensure precision, reliability, and productivity in the process of laser cutting operations.

Chiller: Termotek PU-0600 Chiller

To ensure optimal performance and safe operation of the Trumpf laser, we use the Termotek PU-0600 chiller (Figure 5.23), an industrial-grade cooling and temperature control unit. This chiller maintains stable operating temperatures for both the laser module and the laser cutting head, which is crucial for preventing overheating during continuous high-power operation.

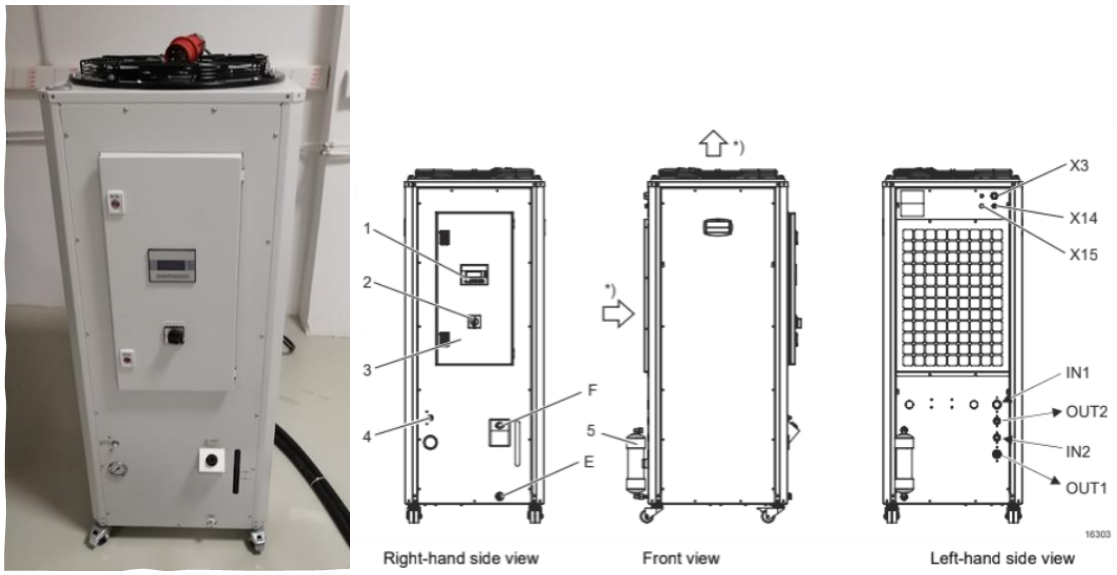


Figure 5.9. Termotek PU-0600 Chiller

The Termotek PU-0600 features a 14-liter coolant tank and dual water circuits, each designed to address specific cooling requirements:

- **Water Circuit 1 (Laser Module):** This primary circuit cools the laser module itself and has a high cooling capacity of 6000 watts. It includes an oscillator that maintains a flow rate of 19 liters per minute at 3 bar pressure or 20 liters per minute at 2.5 bar. The robust flow ensures effective heat removal, keeping the laser module within the required temperature range for consistent power output and accuracy.

- **Water Circuit 2 (Cutting Head):** The secondary circuit is dedicated to cooling the laser cutting head. It has a lower cooling capacity of 100 watts, sufficient to maintain the optical elements of the cutting head at an optimal temperature. A flow rate of 1.5 liters per minute at 2.5 bar prevents overheating of the optics, ensuring that beam quality remains unaffected by thermal influences.

The Termotek PU-0600 chiller provides active cooling for both the laser module and the cutting head, enabling the laser system to perform long-duration, high-precision machining. This stable thermal environment ensures repeatable results and preserves both laser and optical integrity throughout our experiments.

Appendix E - Laser Software

Laser Software: Trumpf Fiberview

The Trumpf Fiberview software provides a comprehensive interface for controlling and fine-tuning the Trumpf high-power laser. It is particularly useful for configuring laser parameters, managing power settings, and monitoring operations. This functionality enables the precise execution of laser-based experiments featured in this thesis, ensuring a high level of accuracy and control.

Laser Control and Laser Parameter Configuration

To control the laser's characteristics, Trumpf Fiberview software, allow to configure critical laser parameters such as intensity, duration, pulse frequency, and power output (Figure 5.10). Fiberview enables to customize the laser's behavior to suit the specific requirements of our experimental processes, as different material processes—such as cutting, engraving, or surface treatment—demand varying laser intensities and exposure times.

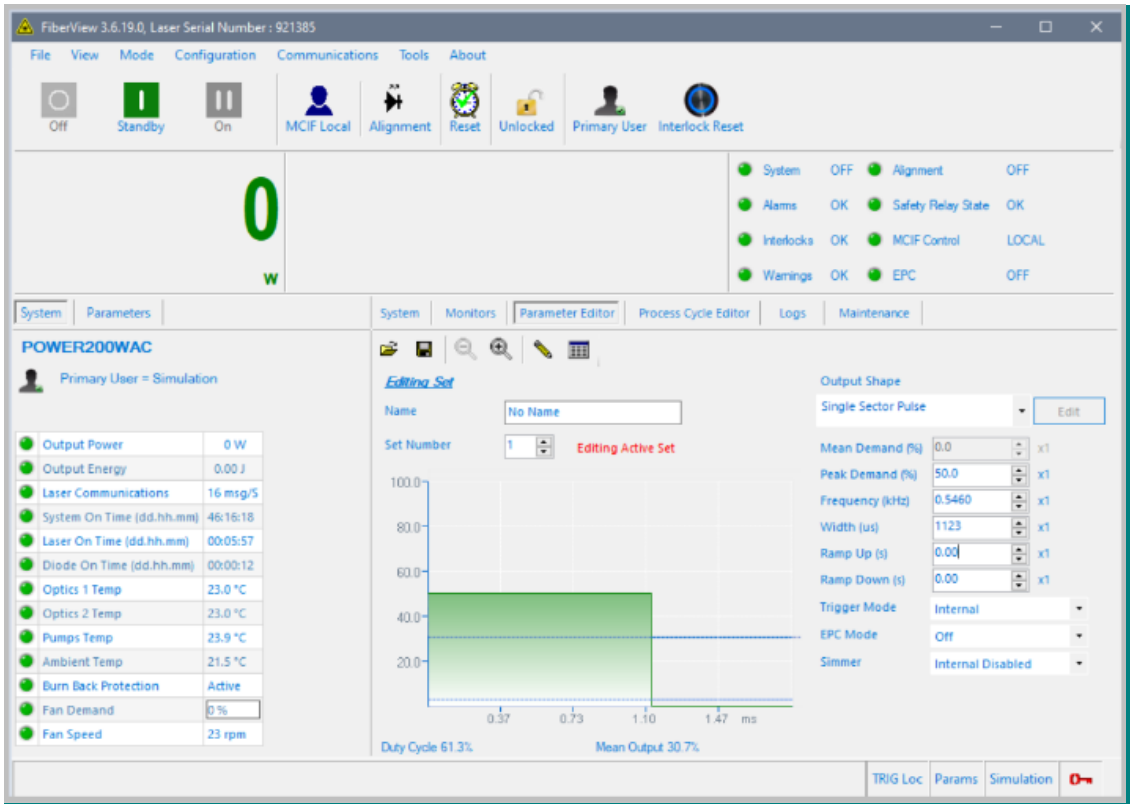


Figure 5.10. Trumpf's Fiberview software interface

With Fiberview, full control of laser operations is possible, from basic on/off functions to power adjustments, along with the creation of complete profiles designed to specific machining applications. The software allows optimization of key laser characteristics such as power intensity, pulse frequency, and pulse duration, enabling detailed control over energy application to the workpiece. This level of control allows us to fine-tune laser performance for applications like cutting or engraving, ensuring that the parameters are optimized to achieve high precision on the Al samples.

In our setup, Fiberview is used in conjunction with Mach3, creating an integrated control system. Fiberview defines the laser's operational parameters, while Mach3 manages the timing and positioning of the laser activation along the CNC path. This dual-software approach offers both flexibility and precision, allowing us to adjust laser settings for different experiments without modifying the CNC path programming. By configuring these parameters in Fiberview and transmitting them to Mach3 through a custom PCB interface, a consistent and precise laser operation during every experimental run is ensured.

Parameter Programming and Pulse Shaping

One of the major features of Fiberview is the ability to program laser parameters with accuracy. Additionally, it allows defining specific pulse shapes and providing independent control over the distribution and timing of energy bursts emitted by the laser. Pulse shaping is particularly important for delicate or variable energy applications, as it enables one to customize how laser energy is applied to a material. This prevents overheating or deformation of the material and ensures the process meets the high-quality standards required for research.

Process Cycles and Parameter Sequencing

The Process Cycle functionality in Fiberview allows the programming of automated sequences, where different laser parameters are applied in a specific order according to the pre-programmed method. This is particularly useful in multi-stage machining operations, where different stages of the process may require varying power, frequency, or even duration. The programmed process cycles enable the continuous execution of multi-stage machining operations without interruption, eliminating the need for manual adjustments between stages. This feature ensures smooth transitions between sets of parameters, saving time while maintaining precision.

Local and networked monitoring

Fiberview provides both local and networked monitoring, allowing operators to control and observe the laser's performance from either a local PC or remotely over a network. This feature is particularly convenient for experiments with remote monitoring, as it enables operators to adjust various laser parameters in real-time without needing on-site access to the physical setup. Additionally, it offers detailed feedback through laser status logs, error reports, and performance data, facilitating easier management and optimization.

Local Servicing and Repair

Another advantage of Fiberview is its integration of servicing and repair functions, enabling operators to quickly diagnose issues and apply maintenance solutions efficiently. It also includes diagnostic tools for local service, helping to maximize the laser equipment's service life. This feature is especially crucial in research applications, where continuous operation and performance are vital to staying on schedule with project timelines.

The advanced control and monitoring features in the Trumpf Fiberview software provide a flexible and robust platform for handling laser machining. Precision controls, automation options, and remote access enable consistent and repeatable results.

Appendix F - Equipment integration

The laser machining system used integrates a Precitec LightCutter 2.0 Motorized 3D laser cutting head mounted onto a Denford Easimill 3 CNC machine (Figure 5.11). The CNC is connected to a computer running Mach3 software, which serves as a versatile interface for controlling CNC movements. Mach3 enables detailed adjustments and synchronization, which are essential for experiments requiring both precision and consistency. This configuration combines the precise motion control of the CNC system with the high-power laser cutting capabilities of the Precitec head, facilitating detailed laser processing of aluminum alloy samples. To ensure proper functionality and precision, the laser cutting head was mounted vertically onto the CNC work bed using a custom-designed bracket (

Figure **5.12**). This bracket securely holds the cutting head in place while maintaining optimal alignment with the workpiece.



Figure 5.11. Precitec LightCutter 2.0 Motorized 3D laser cutting head, mounted onto a

Denford Easimill 3 CNC machine

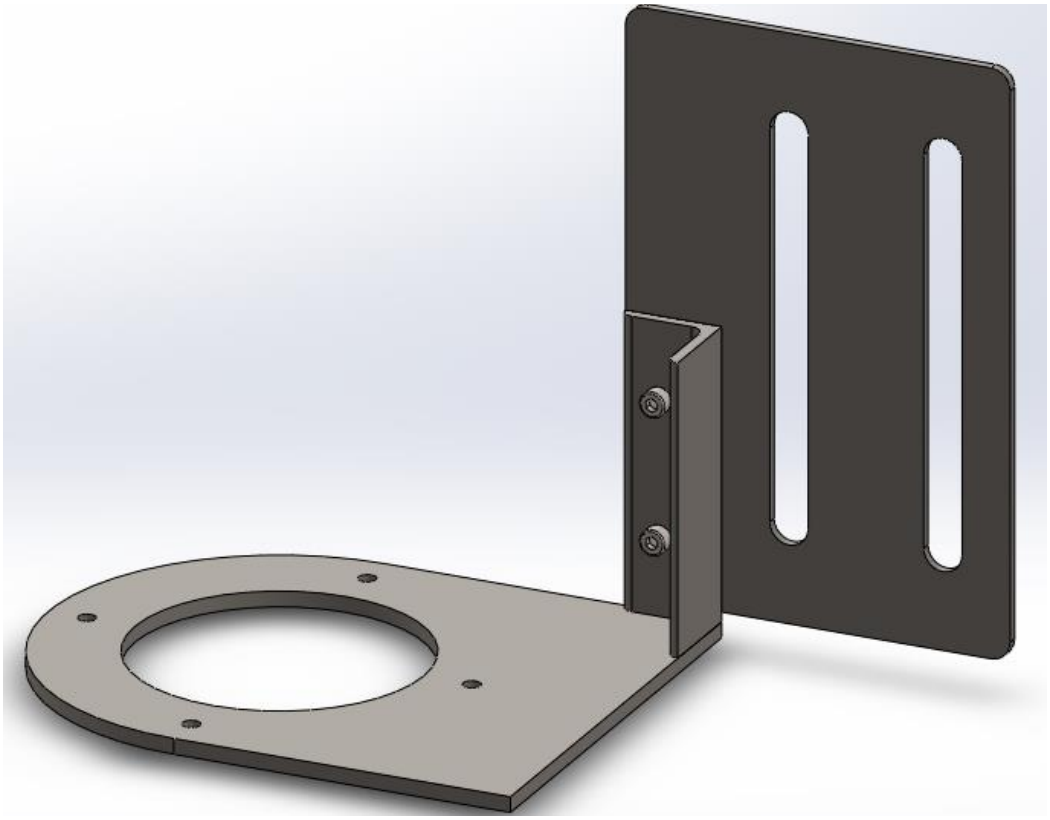


Figure 5.12. Custom-designed bracket using CAD software to vertically mount the Precitec laser cutting head, onto the Denford Easimill 3 CNC machine

Alignment procedure

To achieve perfect vertical alignment of the laser cutting head relative to the work bed, a precise calibration process was conducted using the laser head's probe and alignment beam. The procedure involved placing an optical mirror on the CNC work bed and utilizing a piece of paper with a central hole, functioning as an iris, to aid in the alignment. The objective was to reflect the alignment beam back to the center of the iris, ensuring that the laser beam was precisely perpendicular to the surface of the work bed. Thus:

- The laser cutting head emitted the probe/alignment beam towards the work bed, where the mirror was placed.
- The reflected beam was carefully observed through the hole in the paper (iris).

- By making fine adjustments to the cutting head's position, the alignment beam was calibrated to reflect directly back into the center of the hole, confirming that the laser head was aligned vertically (Figure 5.13).

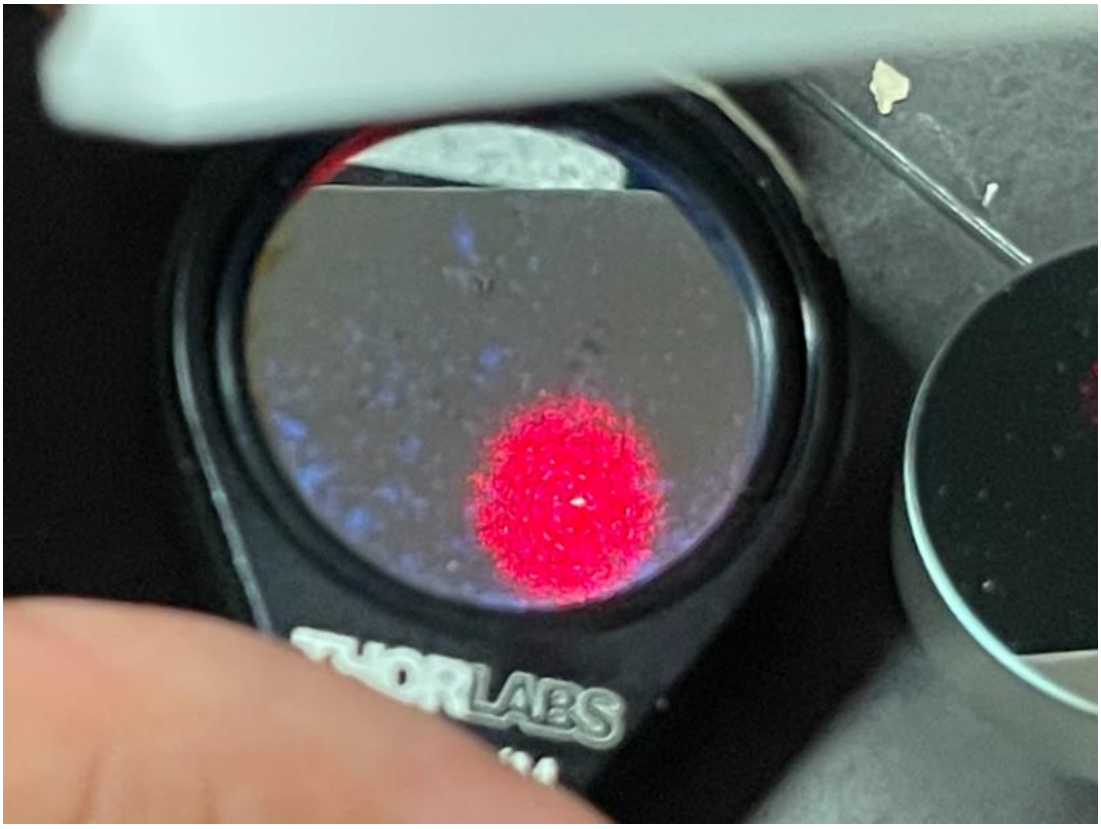


Figure 5.13. Vertical alignment of the Precitec laser head to the cutting work-bed using a mirror perpendicular to the work-bed to center the reflected beam

This alignment procedure is critical for ensuring uniform energy distribution across the laser's focal spot, resulting in more consistent machining outcomes. It is crucial for achieving accurate cuts and engravings, especially when utilizing high-power lasers like the CW Trumpf laser. Any deviation from vertical alignment could lead to irregular cuts, uneven energy absorption, and suboptimal performance during engraving or cutting operations. To further protect the system, the work bed was modified to prevent potential damage during high-power laser cutting. A 20 mm thick steel plate was added to the surface of the CNC bed to act as a protective layer. This steel plate absorbs any excess laser energy that may pass through the material being processed, protecting the CNC machine from unintended cuts, heat damage, or other wear caused by the laser.

Synchronization of CNC-Laser System

The laser machining system integrates a custom-designed PCB board with Mach3 software to synchronize CNC movements and laser operations. The PCB transmits signals to manage laser activation and power settings, ensuring precise and coordinated execution of machining processes. This setup protects the CNC machine during high-intensity operations, enables precise material removal on aluminum alloy samples, and facilitates efficient laser-CNC integration. By utilizing these advanced features, the system provides a stable and adaptable platform for detailed experiments, allowing precise and repeatable results critical for studying laser-material interactions.

G-code Programming for CNC-Laser Operations

Most control in CNC-laser operations is executed using G-code, the industry standard for programming such machines. G-code specifies the path, position, speed, and operational sequences that a CNC tool head follows to perform material removal or modification. Each command in a G-code sequence corresponds to a specific action on the CNC, such as initiating a cut, changing direction, or driving the stepper motors.

In this thesis, G-code is used to synchronize CNC movements with laser activation, as outlined in Table 5.1. This enables the laser machining to be integrated with the CNC path. A custom-designed PCB board installed in the setup receives signals from Mach3 software, which interprets G-code instructions to trigger the laser at exact moments. Thus, it is ensured that the laser activates only when the CNC head is in the correct position. Custom G-codes like Axx and Bxx are used to start, stop, and select subsequent process cycles, while standard G-codes configure the parameters for each program (Figure 5.14). This approach ensures a fully automated and accurate CNC-laser operation, essential for delivering the precision required.

```
G0 G17 G40 G21 G90 G94 G49
X85
Y5
G04 P1000(MSEC)
A0.01
G04 P1000(MSEC)
Y10
G04 P1000(MSEC)
B0.01
B-0.01
G04 P1000(MSEC)
Y15G04 P1000(MSEC)
B0.01
B-0.01
G04 P1000(MSEC)
Y20
G04 P1000(MSEC)
B0.01
B-0.01
G04 P1000(MSEC)
Y25
G04 P1000(MSEC)
B0.01
B-0.01
G04 P1000(MSEC)
Y30
G04 P1000(MSEC)
B0.01
B-0.01
G04 P1000(MSEC)
Y35
G04 P1000(MSEC)
B0.01
B-0.01
G04 P1000(MSEC)
Y40
G04 P1000(MSEC)
B0.01
B-0.01
G04 P1000(MSEC)
A-0.01
Y0
X0
```

Figure 5.14. G-Code sample for linear cutting motion movement switching to multiple laser process cycles

Table 5.1. Mach3 G-code controls used for Laser-CNC operation

G-Code	Description
G0-G01	Linear move
G17	Select workspace plane XY
G40	Cancel cutter compensation commands (G41 & G42)
G21	Metric unit conversion
G90	Absolute positioning system
G94	Feedrate units per minute
G49	Cancel tool length compensation
G04	Dwell (pause)
A0.01	Process cycle start
A-0.01	Process cycle end
B0.01 & B-0.01	Next process cycle (Both commands used together)

Software Integration for CNC-Laser Control system

The integration of Mach3, G-code, and Trumpf Fiberview establishes a unified control system that synchronizes the CNC's mechanical movements with laser activation for precise and repeatable machining. Mach3 acts as the central control hub, where both the CNC path (G-code)

and laser signals are managed. The custom PCB board bridges Mach3 with the laser, receiving the activation commands generated by G-code and Fiberview settings. This architecture ensures that the laser activates only at designated points along the CNC path, with intensity and duration tailored to experimental needs. This setup is essential for achieving accurate and reliable machining results on Al samples, supporting the research objectives of this thesis.

Appendix G - Diagnostic methods and instruments

Diagnostic techniques and tools represent the core methodological instrumentation for both research and industrial practice. They enable the evaluation, monitoring, and optimization of processes and material performance. In manufacturing and engineering, diagnostics are essential for ensuring quality, reliability, and performance through defect detection, property measurement, and the analysis of system behavior under varying conditions. This field includes a wide range of approaches, from non-destructive testing (NDT) methods—such as ultrasonic, radiographic, and thermal imaging—to advanced diagnostic instruments, including spectrometers, scanning electron microscopes (SEM), and laser-based measurement systems.

The diagnostic instruments selected for this study enable precise monitoring and analysis of material behavior and process performance. Thermal cameras and thermocouples are employed to measure temperature distributions during experiments, providing essential data for analyzing thermal behavior. Active strain gauges deliver critical information about deformation and stress in materials, offering valuable insights into mechanical performance under load. White light interferometry facilitates high-resolution surface measurements, allowing for the evaluation of surface roughness and dimensional accuracy. A stereomicroscope is utilized for detailed visual inspection and material characterization, aiding in the identification of defects and changes in microstructure. Together, these diagnostic tools form an integrated approach that enables precise analysis and optimization of processes.

Thermal camera

To evaluate and validate the experimental and simulation results, a precise thermal diagnostic system is utilized. An Optris PI1M thermal camera (f = 75 mm) is mounted on the CNC machine, focusing on the workpiece at 310 mm from the camera sensor (see Figure 5.15). The camera is equipped with two band-rejection Notch filters, arranged in series, to reduce laser beam

reflections, providing an optical density of 12. Additionally, a long-pass filter with a cut-on wavelength of 750 nm is used to capture thermal data at a frame rate of 80 Hz. The material emissivity is calibrated within the camera's software and set to 0.05 for Al 1050. An iris diaphragm is employed to further minimize reflections from the workpiece towards the thermal camera, ensuring accurate thermal measurements.



Figure 5.15. Optris PI-1M thermal camera focused on the irradiated workpiece spot

Optris PI-1M thermal camera specifications are listed in the table below.

Table 5.2. Optris PI-1M Technical details

Attribute	Value
Detector:	CMOS (15µm x 15µm)
Optical resolution / Frame rate:	64 x 480 pixels @ 32 Hz 382 x 288 pixels @ 80 Hz (swichable to 27 Hz) 72 x 56 pixels @ 1 kHz 764 x 8?? pixels @ 1 kHz (fast linescanning mode)

Spectral range:	0.85 – 1.1 μm
Temperature range:	525 … 1800 °C (27 Hz mode) 575 … 1800 °C (80 Hz and 32 Hz mode) 675 … 1800 °C (1 kHz mode)
Lenses:	**FOV @ 382 x 288 px:** 4° x 3° (f = 75 mm) **FOV @ 764 x 480 px:** 9° x 5° (f = 75 mm)
Thermal sensitivity (NETD):	< 2 K (< 900 °C) < 4 K (< 1400 °C)
System accuracy (at ambient temperature 23 ± 5°C) :	Object temperature < 1400 °C: ±1 % for 27/32/80 Hz ±1,5 % for 1 kHz Object temperature < 1600 °C: ±2 % for 27/32/80 Hz ±2,5 % for 1 kHz

Thermocouples

Thermocouples are among the most important temperature-measuring devices due to their high accuracy and responsiveness, particularly in high-temperature applications. In our setup, two thermocouples were positioned 0.5 to 2 millimeters away from the irradiation spot to measure temperatures at specific pre-defined locations. One was a K-type thermocouple, and the other was an N-type. Their close placement within the camera's scanning path allows for real-time monitoring of temperature fluctuations during irradiation, providing detailed thermal profiling. This is crucial for understanding material behavior and optimizing process parameters.

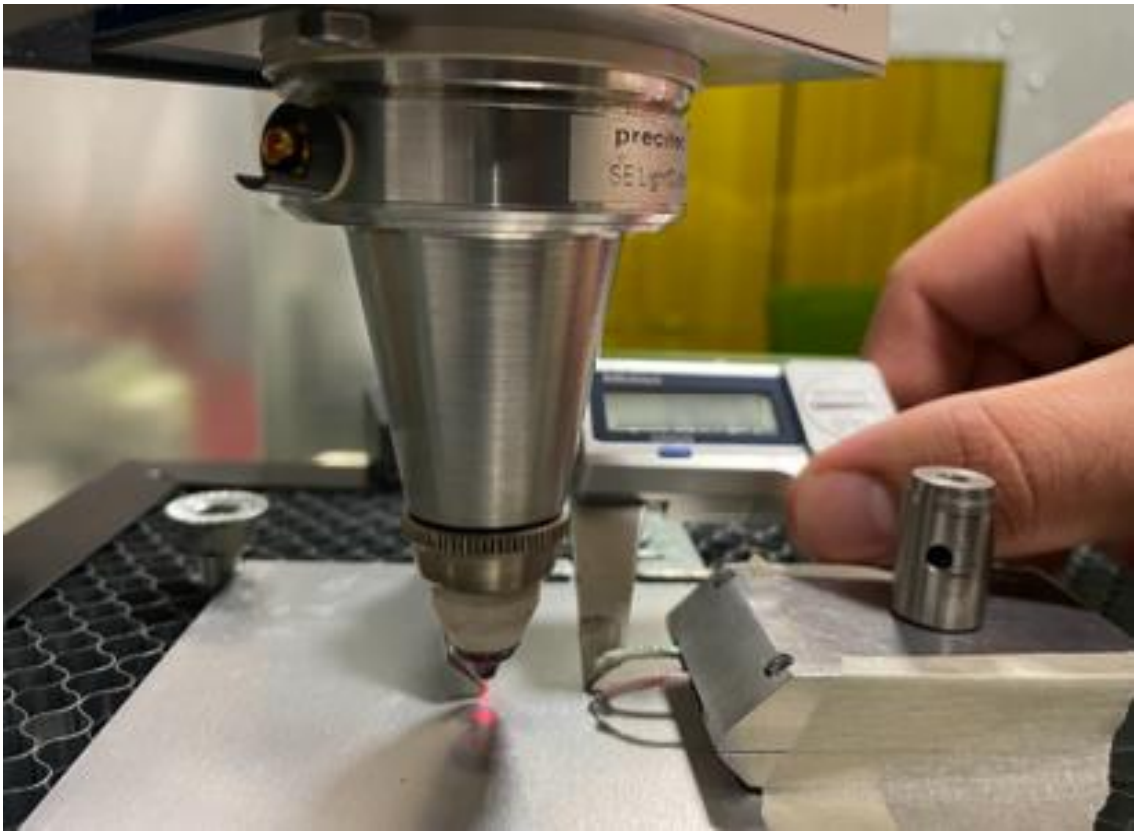


Figure 5.16. Thermocouples mounted on the top surface of the Al workpiece

The thermocouple specifications are listed in the table below.

Table 5.3. RS PRO Type K & Type N thermocouple specifications

Attribute	Value	Value
Thermocouple type:	K	N
Probe Diameter:	0.3 mm	0.3 mm
Probe Length:	2 m	2 m
Probe Material:	Glass Fiber	Glass Fiber
Maximum Temperature Sensed:	+ 600 °C	+ 1200 °C
Response Time:	0.7 s	0.7 s

Strain gauges

Strain gauges are precision instruments used to measure strain, which is the deformation or displacement of a material in response to applied forces. They operate on the principle that electrical resistance changes proportionally to the strain experienced by the material. A typical strain gauge consists of a thin conductive material arranged in a grid pattern and is usually bonded directly to the surface of the material being studied.

When a material deforms due to applied force, the attached strain gauge stretches or compresses, causing a corresponding change in its electrical resistance. Measuring this resistance change allows for the determination of material stress and strain. The high sensitivity of strain gauges, defined by their gauge factor, makes them invaluable for analyzing stress, strain distribution, and load-bearing capacities across various applications.

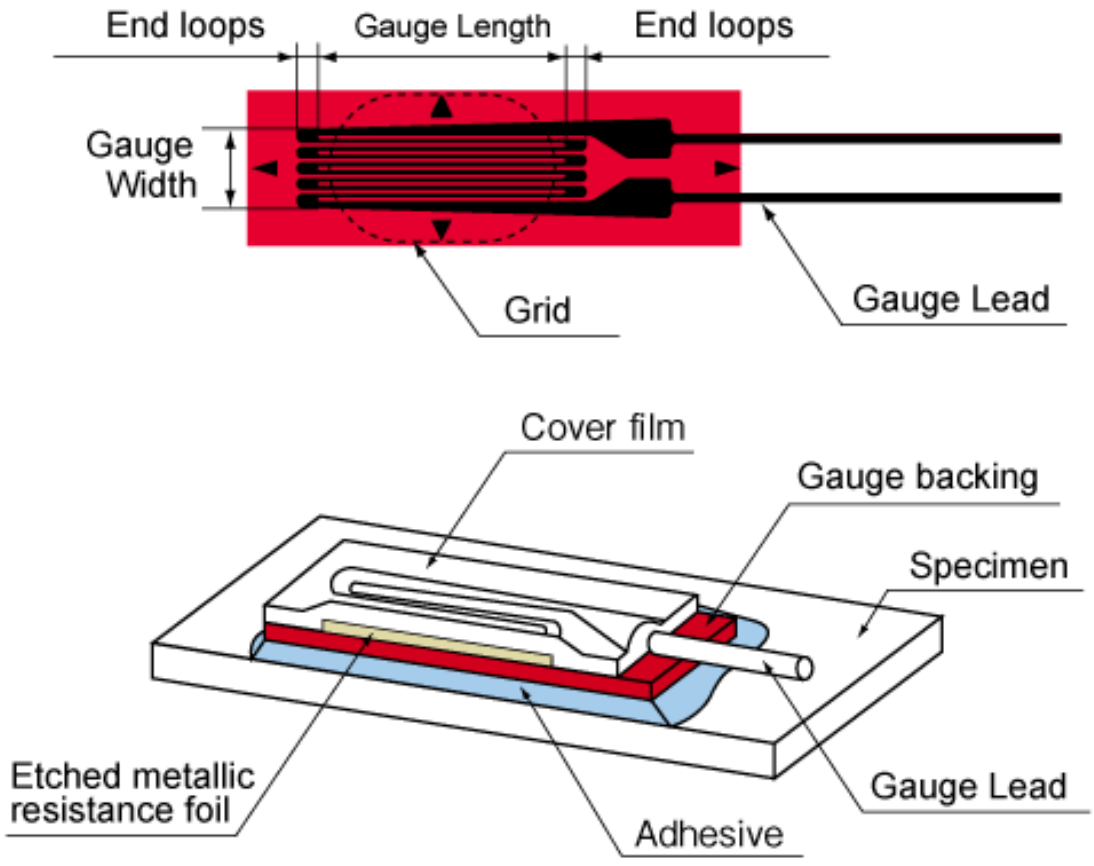


Figure 5.17. Strain gauge construction [22]

White Light Interferometry

WLI is an optical, non-contact measurement technique widely recognized as a reliable method for surface characterization and topography analysis. As the name implies, this technique utilizes the interference of light waves to reconstruct surface features with nanoscale precision. In WLI, white light—a broad-spectrum illumination source—is split into two beams: one reflects off the sample surface, while the other reflects off a reference mirror. These beams then recombine to create an interference pattern, which is analyzed to determine surface heights and features with exceptional accuracy.

WLI is extensively used to study surface roughness, flatness, and dimensional changes under varying conditions. Its high spatial resolution enables the measurement of complex geometries and fine surface details, making it especially suited for applications in laser machining and thermal effect studies. An additional advantage of WLI is its non-destructive nature, which ensures the integrity of delicate materials during analysis. This technique plays a critical role in validating simulation models and optimizing processes by providing precise surface metrics. Due to its versatility and precision, WLI is indispensable in advanced material characterization and quality control.

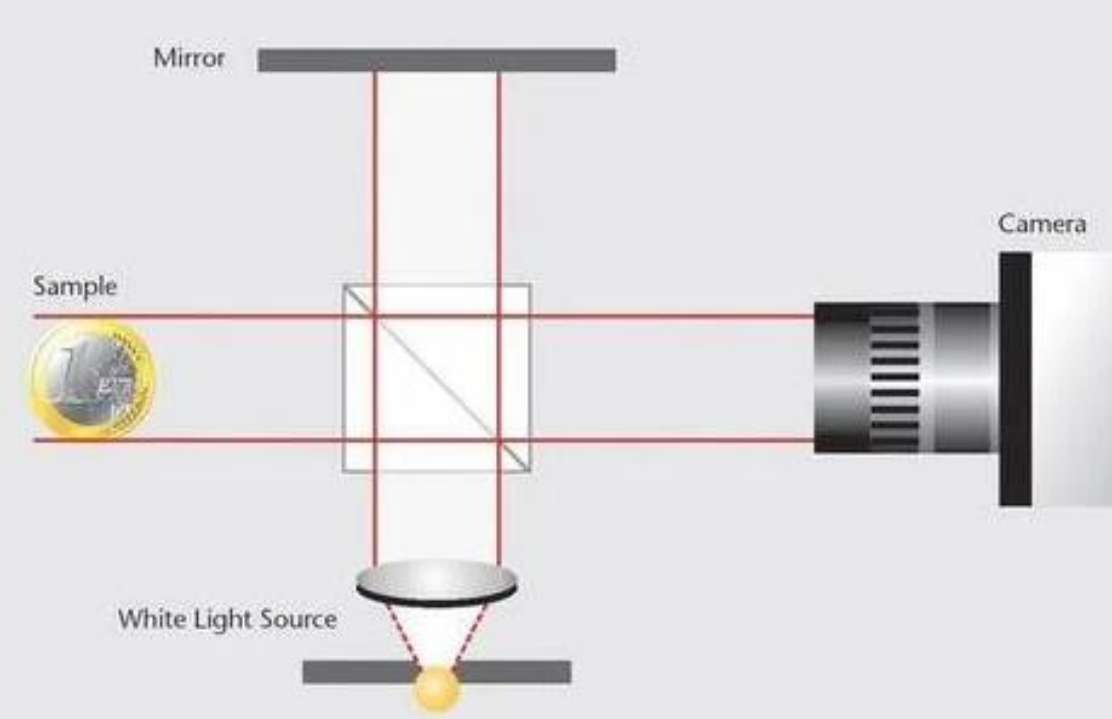


Figure 5.18. White light interferometry setup [2]

Stereomicroscope

Stereomicroscopes are advanced optical instruments designed for detailed visual investigations of materials, focusing on their surface and structural features. Unlike conventional microscopes, a stereomicroscope provides a three-dimensional view of the sample through two separate optical paths. This setup enables excellent depth perception, making it particularly suitable for observing fine and complex surface structures.

In this study, the stereomicroscope is employed to analyze material surface features in detail, enabling the detection of defects, microcracks, and other anomalies that may occur during or after processing. Specifically, the processed aluminum workpieces are examined using a Leica MZ6 stereomicroscope, which offers magnification capabilities ranging from 0.63x to 4.0x. It thus enables both broad overviews and detailed analyses of surface features within its magnification range, making it ideal for assessing details of laser-machined components. The stereomicroscope is particularly valuable for qualitative investigations, where direct observation complements other quantitative testing methods, such as interferometry or thermography. The combination of high magnification and depth perception allows for precise assessments.



Figure 5.19. Leica MZ6 Stereomicroscope

The stereomicroscope's specifications are listed in the table below.

Table 5.4. Leica MZ6 stereomicroscope specifications

Attribute	Value
Magnification:	0.63 0.8 1.0 1.25 1.6 2.0 2.5 3.2 4.0
Eyepieces:	WF 10x/20 goggles
Field diameters:	Up to 104.2 mm
Working distances:	Up to 297 mm

The experiments are conducted in IPPL [24], utilizing all the aforementioned tools, diagnostics, and equipment. The initial goal was to validate the technical specifications provided in the equipment manuals. To begin, single laser shots were performed to confirm the correct positioning of the laser cutting head. This was achieved using IR paper and conducting shots at varying focal distances (**Figure 5.20**).



Figure 5.20. Laser shots on IR paper were compared to a 250 μm copper sample, observed through a stereomicroscope

The experimental setup utilized the CNC machine, and the irradiated workpiece was a 1 mm thick Al 1050 H14 sheet. The experiments were conducted at room temperature (20 °C) under atmospheric conditions. Initially the experimental setup was designed to model square metal plates of 100 mm x 100 mm, as shown in **Figure 5.21**. The workpiece was secured using a washer and locking nut on both the top and bottom sides.

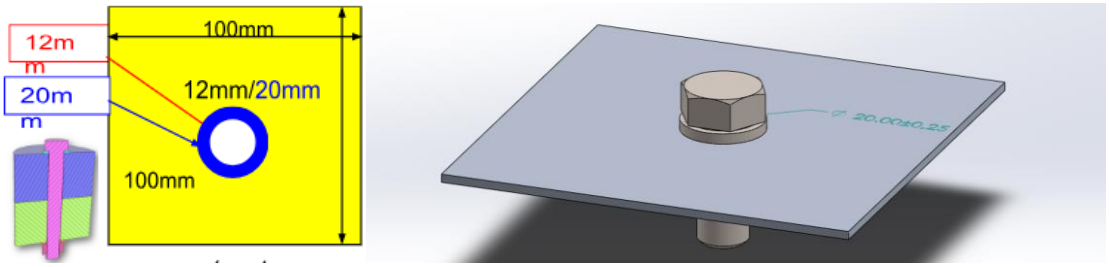


Figure 5.21. CAD modeled workpiece secured with washer (d=20 mm) and a locking nut on top/bottom sides through a d=12 mm hole diameter

After several preliminary tests and experiments, the experimental setup was modified, as the stress and strain developed on the workpiece altered the results (**Figure 5.22**).

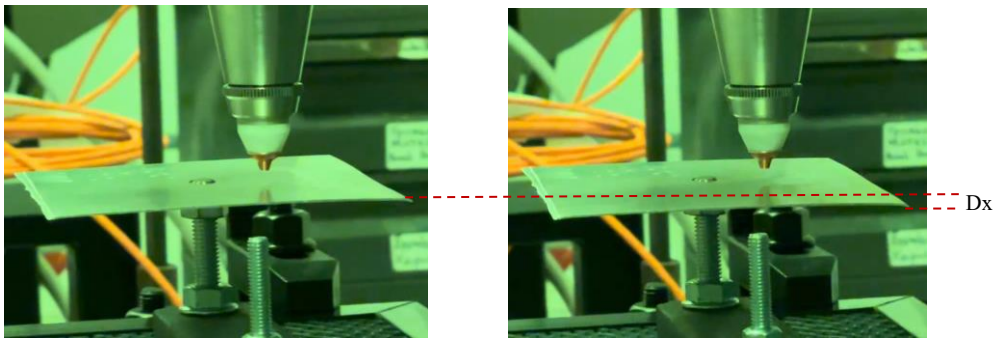


Figure 5.22. The stress applied by the nut on the workpiece caused a displacement of Dx during laser irradiation, altering the results.

To protect the experiment from external forces, the workpieces were placed on a metallic mesh grid, ensuring no additional forces influenced the process (Figure 5.23).



Figure 5.23. Workpiece positioned on top of a metallic grid mesh

The thermal camera was positioned above the setup and focused on the laser-irradiated spot to capture experimental data for later evaluation. To ensure accurate thermal readings, a needle was heated using a lighter, and the optimal focus distance for the thermal camera was determined to be 92 mm from the front lens cover (Figure 5.24).

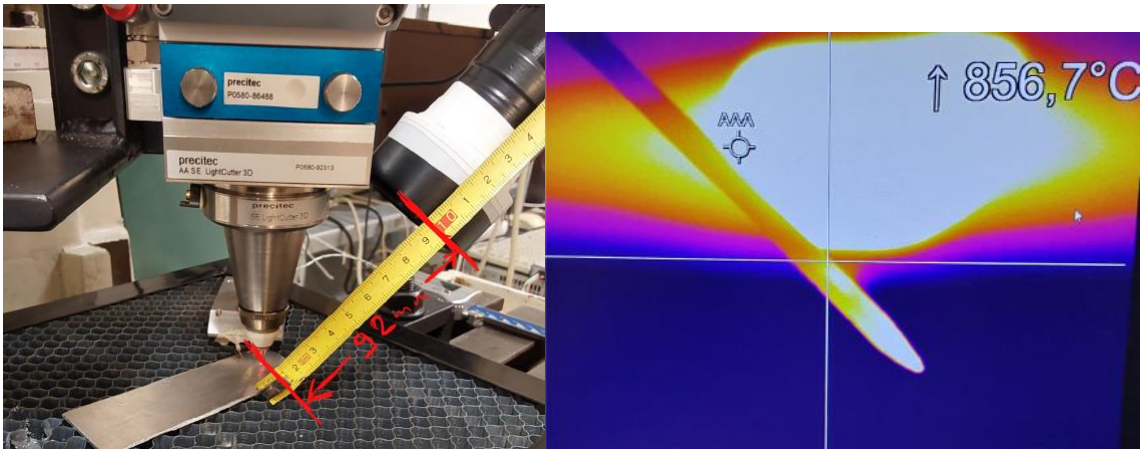


Figure 5.24. Thermal camera focused at 92 mm distance on a heated needle

From the thermal camera manual specifications, we know that the camera's magnification is ×0.45. We determined that the thermal camera's field of view along the horizontal axis is 12.5 mm using the following equation

$$magnification = \frac{chip\ dimension}{real\ image} \quad (1)$$

We then calibrated the emissivity within the thermal camera and validated the thermal readings by using the flame from a lighter (Figure 5.25) which is approximately around 1000 °C [20] according to the literature.

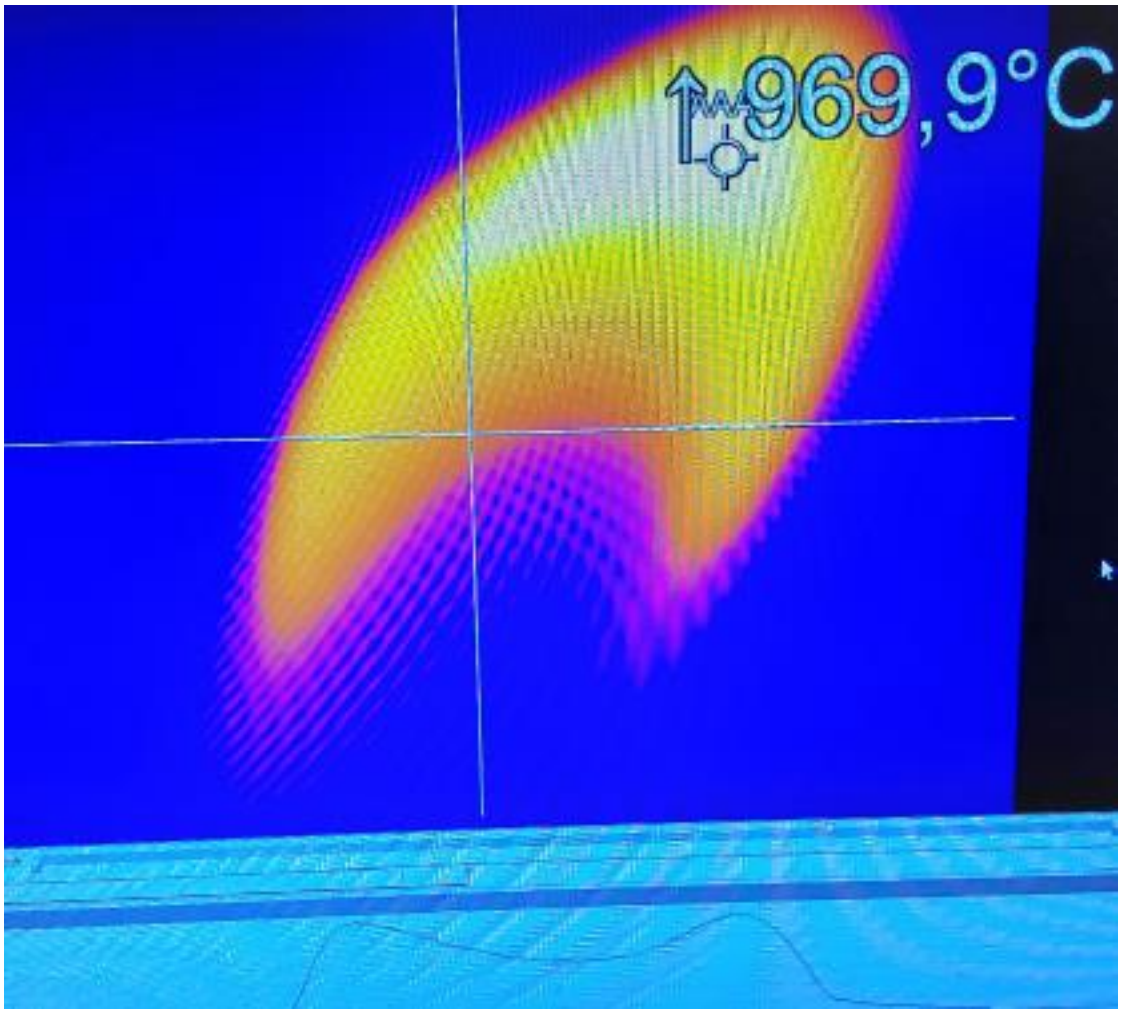


Figure 5.25. Thermal image of a lighter flame showing temperature of 969.9 °C

References

[1] https://en.wikipedia.org/wiki/Laser

[2] DUTTA MAJUMDAR, J.; MANNA, Indranil. Laser material processing. International materials reviews, 2011, 56.5-6: 341-388.

[3] NATH, A. K. High power lasers in material processing applications: an overview of recent developments. Laser-assisted fabrication of materials, 2012, 69-111.

[4] R. Paschotta, article on "Laser Material Processing" in the RP Photonics Encyclopedia, retrieved 2025-02-09, https://doi.org/10.61835/wnq

[5] Zienkiewicz, O.C., Taylor, R.L., Zhu, J.Z. The Finite Element Method Set, 6th edition Elsevier Butterworth-Heinemann, Oxford, UK (2005)

[6] KASELOURIS, Evaggelos; DIMITRIOU, Vasilis. Vibro-acoustics time domain FEM-BEM analysis of a Titian Stradivari violin: the role of the bridge. In: Journal of Physics: Conference Series. IOP Publishing, 2023. p. 012009.

[7] KASELOURIS, E.; DIMITRIOU, V. Study of transient wave and vibro-acoustic response of a cymbal during laser impact via FEM-BEM numerical simulations. In: AIP Conference Proceedings. AIP Publishing, 2023.

[8] KASELOURIS, E., et al. A review of simulation methods of laser matter interactions focused on nanosecond laser pulsed systems. Journal of Multiscale Modelling, 2013, 5.04: 1330001.

[9] K. Y. Nyon, C. Y. Nyeoh, M. Mokhtar & R. Abdul-Rahman, Finite element analysis of laser inert gas cutting on Inconel 718, Int. J. Adv. Manuf. Technol. (2012) 60:995–1007.

[10] HE, Xiaocong. Finite element analysis of laser welding: a state of art review. Materials and Manufacturing Processes, 2012, 27.12: 1354-1365.

[11] LUO, Zhibo; ZHAO, Yaoyao. A survey of finite element analysis of temperature and thermal stress fields in powder bed fusion Additive Manufacturing. Additive Manufacturing, 2018, 21: 318-332.

[12] LEMU, H. G. Multiphysics modeling and numerical simulation in computer-aided manufacturing processes. Metals, 2021, 11: 175.

[13] ALAVALA, Chennakesava R. Finite element methods: Basic concepts and applications. PHI Learning Pvt. Ltd., 2008.

[14] Rao, S. S. (2011). Chapter 2: Discretization of the Domain. In The Finite Element Method in Engineering (pp. 53–73).
[15] SHAH, Qasim; ABID, Hasan. LS-DYNA for beginners: an insight into LS-PrePost and LS-DYNA. (No Title), 2012.
[16] https://www.hpc.grnet.gr/en/
[17] KASELOURIS, Evaggelos, et al. (2013) 3D FINITE ELEMENT MODELING OF LASER-GENERATED SURFACE ACOUSTIC WAVES IN FILM-SUBSTRATE SYSTEMS VALIDATED BY EXPERIMENTS, 10th HSTAM International Congress on Mechanics, Chania.
[18] Ciornei, D., Popa, A., & Munteanu, C. (2017). "Mechanical properties and microstructure of aluminum alloys: Influence of cold working and heat treatment." Journal of Materials Processing Technology, 246, 77-84.
[19] Indhu, R., et al. "Overview of laser absorptivity measurement techniques for material processing." Lasers in Manufacturing and Materials Processing 5 (2018): 458-481
[20] https://www.papirmass.com/how-hot-is-fire-from-a-lighter/
[21] CHRYSSOLOURIS, G.; ANIFANTIS, N.; KARAGIANNIS, S. Laser assisted machining: an overview. 1997.
[22] NASTRI, Elide, et al. First exploring the cyclic behaviour of aluminium beams under non-uniform bending: Experimental and FE analysis. Engineering Structures, 2025, 322: 119144.
[23] https://www.azooptics.com/Article.aspx?ArticleID=1204
[24] Computer Numerical Control of a 3-Axis Milling Machine for Continuous Wave Laser Machining Processes, S. Kamposos, MSc Thesis, 2025, Rethymno, Greece.
[25] Zhang, Y., Zhang, W., & Li, L. (2018). Ablation characteristics and surface morphology in laser marking of metals. Optics & Laser Technology, 104, 72–80.
[26] J. R.Lawrence, ed. Advances in laser materials processing: technology, research and applications. Woodhead Publishing, 2017.
[27] Shin, Yung C., et al. "Overview of laser applications in manufacturing and materials processing in recent years." Journal of Manufacturing Science and Engineering 142 (2020) 110818.
[28] Serguei P. Murzin, and C. Stiglbrunner. Fabrication of Smart Materials Using Laser Processing: Analysis and Prospects. Appl. Sci. 14 (2023) 85.

[29] Dutta Majumdar, J., and Indranil Manna. "Laser material processing." International materials reviews 56.5-6 (2011): 341-388 [30] Zhang, Y., Zhang, W., & Li, L. (2018). Ablation characteristics and surface morphology in laser marking of metals. Optics & Laser Technology, 104, 72–80.

[30] Nath, A. K. "High power lasers in material processing applications: an overview of recent developments." Laser-assisted fabrication of materials (2012): 69-111.

[31] Shiner, A. Advances in High-Power Fiber Lasers. Optics and Photonics Journal, 8(3), (2020) 124-136.

[32] L. D. Scintilla, L. Tricarico. Fusion cutting of aluminum, magnesium, and titanium alloys using high-power fiber laser. Optical Engineering 52 (2013) 076115-076115.

[33] C. Wandera, A. Salminen, V. Kujanpaa. Inert gas cutting of thick-section stainless steel and medium-section aluminum using a high-power fiber laser. Journal of laser applications 21 (2009) 154-161.

[34] Lauro, Carlos H., et al. Finite element method in machining processes: a review. Modern Manufacturing Engineering (2015): 65-97.

[35] V. Dimitriou, E. Kaselouris, Y. Orphanos, M. Bakarezos, N. Vainos, I. K. Nikolos, M. Tatarakis, N. A. Papadogiannis, The thermo-mechanical behavior of thin metal films under nanosecond laser pulse excitation above the thermoelastic regime, Appl. Phys. A118 (2015) 739-748.

[36] E. Kaselouris, I.K. Nikolos, Y. Orphanos, E Bakarezos, N. A. Papadogiannis, M. Tatarakis, V. Dimitriou, Elastoplastic study of nanosecond-pulsed laser interaction with metallic films using 3D multiphysics fem modeling, Int. J. Damage Mech. 25 (2016) 42-55.

[37] E. Kaselouris, A. Skoulakis, Y. Orphanos et al. Analysis of the heat affected zone and surface roughness during laser micromachining of metals. Key Engineering Materials 827 (2020) 122-127.

[38] https://www.engineeringtoolbox.com/radiation-heat-emissivity-aluminum-d_433.html

[39] R. Indhu, et al. Overview of laser absorptivity measurement techniques for material processing. Lasers in Manufacturing and Materials Processing 5 (2018): 458-481.

[40] Liu, Huagang, Wenxiong Lin, and Minghui Hong. Surface coloring by laser irradiation of solid substrates. Apl Photonics 4.5 (2019).

[41] MatMake, n.d. Aluminum 1050 properties. Available at:https://matmake.com/materials-data/aluminum-1050-properties.html

[42] Davis, J. R. (1993). Aluminum and Aluminum Alloys. ASM International. ISBN: 9780871704962.

[43] Hallquist, J. O. (2006). LS-DYNA Theory Manual. Livermore Software Technology Corporation. ISBN: 9780971953615.

[44] Semak, V. V., & Matsunawa, A. (1997). The role of recoil pressure in energy balance during laser materials processing. Journal of Physics D: Applied Physics, 30(18), 2541–2552. https://doi.org/10.1088/0022-3727/30/18/004.

[45] Dally, J. W., & Riley, W. F. (1991). *Experimental Stress Analysis* (3rd ed.). McGraw-Hill.

[46] Leach, R. K. (2011). *Optical Measurement of Surface Topography*. Springer. https://doi.org/10.1007/978-3-642-12012-2

[47] Leica Microsystems. (n.d.). Leica MZ6 Stereo Microscope – User Manual and Technical Specifications. Leica Microsystems GmbH.